Journal of Membrane Science 658 (2022) 120731

Contents lists available at ScienceDirect

Journal of Membrane Science

journal homepage: www.elsevier.com/locate/memsci

Molecular insights into the structure-property relationships of 3D printed polyamide reverse-osmosis membrane for desalination

Jinlong He [a], Jason Yang [b], Jeffrey R. McCutcheon [c], Ying Li [a,d,*]

[a] Department of Mechanical Engineering, University of Connecticut, Storrs, Connecticut, 06269, United States
[b] Division of Chemistry and Chemical Engineering, California Institute of Technology, Pasadena, CA, 91125, United States
[c] Department of Chemical & Biomolecular Engineering, Center for Environmental Sciences and Engineering, University of Connecticut, Storrs, Connecticut, 06269, United States
[d] Department of Mechanical Engineering and Polymer Program, Institute of Materials Science, University of Connecticut, Storrs, Connecticut, 06269, United States

ARTICLE INFO

Keywords:
3D-printed PA RO membrane
Water desalination
Pore size distribution
Cross-linking degree
Compressive yield strength
Non-equilibrium molecular dynamics

ABSTRACT

3D-printing is an emerging method for manufacturing polyamide (PA) reserve osmosis (RO) membranes for water treatment and desalination, which can precisely control membrane structural properties, such as thickness, roughness, and resolution. However, the synthesis-structure (i.e., degree of cross-linking (DC), m-phenylenediamine/trimesoyl chloride (MPD/TMC) ratio, and membrane thickness) to property (permeability and water-salt selectivity) relationships for these membranes has not been well understood. At the same time, a microscopic understanding of the physical mechanism of water and salt transport is needed to guide the design of high-performance 3D-printed membranes and improve the printing efficiency. Thus, the atomic-scale transport features and energetics of water and salt ions are studied at high pressure for the 3D-printed PA RO membranes with the different DCs and MPD/TMC ratios through non-equilibrium molecular dynamics (NEMD) simulations. Factoring in membrane structure properties, rejection ratio of salt ions and pressure-dependent water flux, 3D-printed PA membranes having an MPD/TMC ratio of 3.0:2.0 and a DC between 80%~90% attains ideal performance: high water flux, high rejection of salt ions, and excellent structural integrity. Mechanistically, water permeability for highly cross-linked PA RO membranes depends on the temporary on-and-off channels that allow water molecules to jump from one cavity to another at high pressure. In addition, higher pressures cause rapid compaction of PA membranes' free volume and membrane thickness. Membrane failure at high pressure is determined by the DC and MPD/TMC ratios-dependent compressive yield strength. In short, these findings provide physical insights for optimizing existing PA membranes and designing next-generation desalination membranes at the molecular level.

1. Introduction

Desalination is a critical technology for augmenting the water supply in many regions of the planet with limited access to freshwater [1–3]. Currently, the industry-standard process for desalination is pressure-driven reverse osmosis (RO) [4–6], where saline water is driven through a membrane with very high salt rejection. The industry-leading RO membrane consists of a thin-film composite (TFC) selective layer [7], which is supported by a polysulfone structure layer. Specifically, the TFC layer is a polyamide (PA) formed via the cross-linking of m-phenylenediamine (MPD) and trimesoyl chloride (TMC) [8]. In industry and most research laboratories, this is accomplished via interfacial polymerization (IP), where MPD is prepared in an aqueous solution while TMC is prepared in the organic solvent, and polymerization occurs at the interface of the mixtures, as these two phases are immiscible. IP can generate a TFC layer that is dense enough to separate salt ions but thin enough to allow water to permeate at reasonable rates [9]. Research to improve RO membranes is primarily focused on increasing selectivity without sacrificing permeability [10–12]. As a result of their outstanding performance in this regard, PA RO membranes formed via IP have been the gold standard in the desalination industry for decades.

Still, IP faces certain inherent limitations. Namely, the reaction is self-terminated so uncontrolled film growth can result in membranes with undesired thickness and rough surface morphology [13–16]. The properties of the support-layer surface can also lead to inconsistent polymerization behavior, with undesirable consequences to membrane

* Corresponding author. Department of Mechanical Engineering, University of Connecticut, Storrs, Connecticut, 06269, United States.
E-mail address: ying.3.li@uconn.edu (Y. Li).

https://doi.org/10.1016/j.memsci.2022.120731
Received 21 March 2022; Received in revised form 27 May 2022; Accepted 9 June 2022
Available online 18 June 2022

Abbreviations

PA	Polyamide
RO	Reverse osmosis
MPD	m-phenylenediamine
TMC	Trimesoyl chloride
NEMD	Non-equilibrium molecular dynamics
LJ	Lennard-Jones
DC	Degree of cross-linking
PSD	Pore size distribution
TFC	Thin-film composite

performance [17,18]. Furthermore, film roughness can exacerbate fouling, resulting in significant performance and operational costs for desalination [19]. Several microscopic studies have further found that the PA RO membranes formed via IP have heterogeneous atomic compositions, cross-linking densities, and microstructures along the thickness direction [20–24].

Various manufacturing techniques have emerged to overcome these challenges in PA membranes. For instance, Gu et al. [25] and Karan et al. [26] fabricated layered PA membranes with homogenous composition and structure throughout the membrane by using the molecular layer-by-layer (mLbL) assembled approach. However, the latter was demonstrated for organic solvent nanofiltration rather than desalination. Perreault et al. functionalized graphene oxide nanosheets to PA RO membranes for antimicrobial properties to reduce fouling [27]. Most promisingly, Chowdhury et al. developed a 3D printing method for PA RO membranes using electrospray as an alternative to IP [28]. The electrospray method deposits MPD and TMC as nanoscale droplets while allowing for homogeneous membrane polymerization that is more scalable than other methods [29]. Compared with conventional manufacturing approaches, such as interfacial polymerization, the significant progress for 3D printing techniques toward greater scalability, better material processability, higher speed, and improved resolution have been explored in the formation of specifically designed PA membranes as they are compatible with common membrane materials [30].

With the enhanced tunability offered by 3D printing method, there is of increased importance to understand how membrane chemical composition should be tuned for ideal membrane performance (high permeability and selectivity) and the structural reasons for this. For example, many experimental protocols use a ratio of 4:1 of MPD/TMC for forming the PA layer [28,31–33], but the stoichiometry of the polymerization reaction requires a ratio of 3:2. The impact of having an excess of MPD or TMC should thus be examined. Additionally, it is understood that membranes must reach a certain degree of crosslinking (DC) such that they are dense enough to be selective against salt [34–37]. However, it is unclear the optimal DC for high selectivity without sacrificing significant water permeability. Overall, experimentally capturing the internal structure and dynamics of water and solutes is difficult, which has made a fundamental understanding of optimized membrane transport elusive [38].

Molecular dynamics (MD) simulation is a powerful method to elucidate the microstructural characteristics of membranes and the mechanistic impacts of synthesis conditions on transport properties [39,40]. The first challenge in simulating pressure-driven RO desalination is generating a realistic MD model of the PA membrane. The PA membrane must be accurately crosslinked and hydrated [41]. Many researchers have then used MD to simulate pressure-driven RO desalination and understand the dynamics of water and solutes through PA membranes [42–44]. Nevertheless, many of these studies have failed to arrive at realistic atomic compositions and DCs. Additionally, as viewed through the pore size distribution, many structures were inconsistent with one another. Zhang et al. improved upon the existing methods by developing a repeatable and realistic MD model for PA membranes, which can reproduce the atomic composition, structure, and properties of dry and hydrated PA RO membranes in experiments [45]. Furthermore, their flexible method allowed them to tune the MPD/TMC ratio of the membrane during *in silico* fabrication. The authors further studied water transport dynamics and membrane swelling properties with their realistic membrane models. Still, many aspects of the composition-property relationships of PA membranes remain underexplored. For example, no studies have considered more extensive ranges of MPD/TMC ratios (such as those used in many experimental protocols), and DC has not been systematically varied to determine the ideal cutoff. These property-optimized compositions should then be explained through more a comprehensive structural analysis of the membrane. Finally, with increased interests in high-pressure RO [46–48], it is essential to determine the mechanical strength and effects of applied pressure on structural characteristics for various chemical compositions of PA membranes.

In this work, we use non-equilibrium MD (NEMD) to elucidate the composition-property relationships of PA RO membranes, intermediated by detailed microstructural analysis. We generate realistic dry and hydrated *in silico* membranes to model the 3D-printed PA membranes, based on the procedure implemented by Zhang et al. [45]. We systemically vary both the MPD/TMC ratio from 1:4, 1:1, 3:2 to 4:1 and the DC in the range of 40–96%. We find that an MPD/TMC ratio of 3:2 is ideal, as any stoichiometric excess of molecules can result in a less unimodal pore-size distribution, which compromises selectivity and mechanical strength under high pressure. We also determine that 80–90% DC achieves total salt rejection in our MD simulation timescale, with high water permeability. These findings are further explained via structural and dynamic matrices, such as water flux, salt rejection, microstructure, dynamics behavior of water and salt ions, which is an essential benchmark for assessing the quality of PA membrane fabrication. Interestingly, we notice a significant membrane contraction by simulating desalination at high pressures, which indicates that membrane compaction is also an important element affecting membrane properties during pressurized membrane processes [47]. With growing alternatives to IP of PA RO membranes that offer unprecedented tunability [29,49], such as 3D-printing and mLbL assembly, our study provides a fundamental structural explanation of how composition impacts water and salt transport of PA membranes. Practically, we determine the optimal membrane composition for the fabrication and manufacturing of these membranes, which can serve as an impactful quality-control standard.

2. Computational model and methods

2.1. Atomic models for PA RO membranes

3D-printing method, as shown in Fig. 1(a), is experimentally revealed to produce the PA membranes using electrospraying [28]. The rotating drum is located on the ground and connected to the two separate needles for this technique. One needle spurts the TMC solution, and the other extrudes the MPD solution. TMC monomers are in hexane solution, and MPD monomers are in the water. During the printing process, MPD and TMC monomers were held at a given molar ratio. As monomer solutions flowed from the needle tips, they sprayed and deposited onto the collector surface and randomly reacted upon contact with each other. The needle stage traverses along the collector surface to ensure the solutions cover the whole substrate. Next, the 3D-printing process was performed until the desired PA membrane thickness was obtained.

It can be found that 3D-printing process also includes the IP process. Even though these manufacturing methods include the IP process, their manufacturing procedures essentially show significant differences. For TFC membranes experimentally fabricated by the IP method [51], two reactive monomers conduct the polymerization reaction at the interface

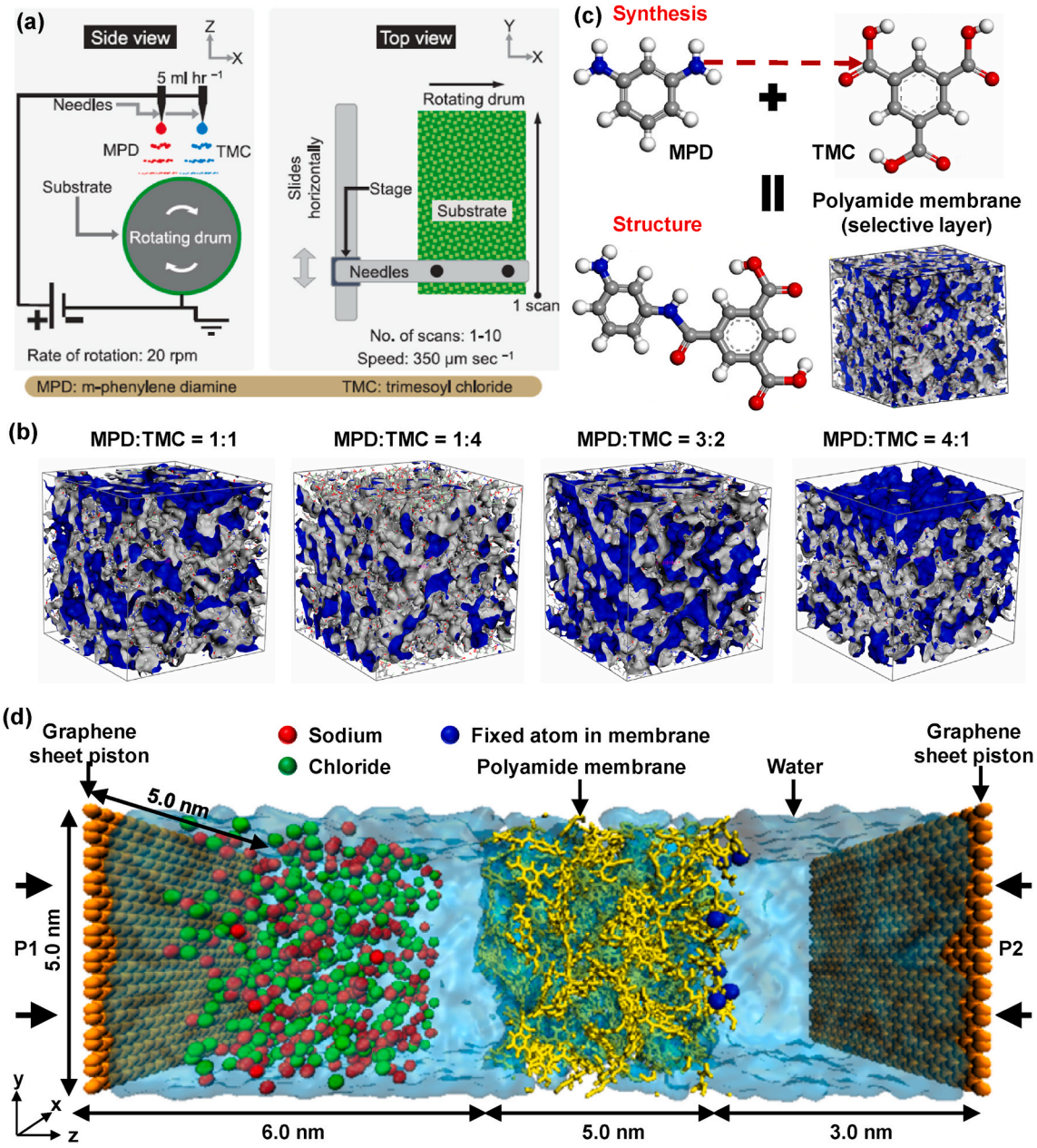

Fig. 1. (a) The side and top view of a schematic of the electrospray process used to fabricate the 3D-printed membranes [28]. (b) PA membrane models with four MPD/TMC ratios, 1.0:1.0, 1.0:4.0, 3.0:2.0 and 4.0:1.0, when polymerization reactions reach 100%, 100%, 90%, and 100% conversion, respectively. (c) Chemical structure of MPD, TMC monomers, and the cross-linking reaction process. (d) MD simulations setup visualized by VMD [50], showing the placement of PA membrane (yellow) with a thickness of 5 nm between two graphene sheet pistons (orange). To improve the visibility of salt ions (e.g., sodium and chloride ions), water molecules are visualized as a light-blue transparent surface. In addition, a small number of atoms (highlighted in blue) located at the permeate side are fixed to mimic the attachment on a substrate. Hydraulic pressure (P1) is applied to the left graphene sheet during the simulation, and standard atmosphere pressure (P2) is exerted on the right graphene sheet. (For interpretation of the references to color in this figure legend, the reader is referred to the Web version of this article.)

between two immiscible solvents. These reactants are composed of TMC and MPD monomers, dissolved in organic solvent and aqueous solution, respectively. A microporous supporting, typically polysulfone, is located at the aqueous MPD solution. Then the supporting film is pushed into contact with the organic TMC solution. The MPD component diffuses into the organic solvent, but the TMC monomers are insoluble in water and stay in the organic solvent. As a result, the polymerization reaction performs in the organic solvent at and near the interface between the two solvents. The reaction is self-limiting because the forming PA becomes an obstacle to the intermixing of the reactants.

Compared with the two manufacturing procedures, we can find that 3D-printing can give more homogeneous reactive sites throughout the whole membrane. However, IP only allows the reaction at the interface between MPD and TMC monomer layers, leading to more inhomogeneous reactive sites. Our 3D-printing simulation models would like to present these unique features in this study. Additionally, to guide the 3D-printing and improve the printing efficiency, it is crucial to understand how some structural factors, such as DCs and MPD/TMC ratios, influence the performance of 3D-printed membranes.

To mimic the experimental 3D-printing process, we computationally generate a crosslinked polymeric PA RO membrane using a multi-step cross-linking procedure [52]. Experimentally, solvent molecules should flow out into the solutions during experimental treatment [53]. Therefore, explicit solvent molecules should not significantly affect the

properties of the resulting PA membrane. However, additional interactions between solvents and membranes, which may slow down the diffusion of monomers, could lead to a very slow polymerization reaction and increase the computational cost dramatically. Therefore, polymerization reaction simulations were carried out in a vacuum without explicit water and other solvent molecules to reduce the computational cost. Taking the example of PA membrane with 90% DC and MPD/TMC ratio of 3.0:2.0, reactive atoms are first assigned to MPD and TMC monomers, as shown in Fig. 1(c). Then employing a cross-section size of 5 nm × 5 nm and a target density of 1.20 g cm^{-3}, 300 MPD and 200 TMC monomers are packed into a 3D-periodic amorphous cell in which TMC and MPD monomers can move randomly in the simulation box. There are 600 potential reaction sites (two for each MPD monomer and three for each TMC monomer). Next, geometry optimization and 5 annealing cycles are exerted for the packed system with periodic boundary conditions in the *x* and *y* directions but for a vacuum in the *z*-direction.

Notably, the multi-step cross-linking procedure used in 3D-printing is similar to those used in other preparation techniques, such as interfacial polymerization (IP) and molecular layer by layer (mLBL). However, 3D-printing leads to a significant difference in that the cross-linking reactions are available throughout the whole membranes instead of across the interfacial regions for the interfacial polymerized PA membranes. The optimized structure is then cross-linked under the canonical (NVT) ensemble with an initial cutoff distance of 4.5 Å. Covalent bonds are created between reactive atoms of acyl carbon and amino nitrogen within the cutoff distance, and the cross-linked network is relaxed under the isothermal–isobaric (NPT) ensemble for 500 ps to update the configuration state. After that, the next cross-linking step continues with an increasing cutoff distance of 0.5 Å until the DC reaches 90%. Besides, at each cross-linking step, the DC is also calculated. The DC is defined as the percent as follows: DC (%) = 100* (number of the formed C − N bonds /number of the possible C − N bonds). After the cross-linking stops, the final DC can be obtained. When the final DC is satisfied, the cross-linking process stops further bond breaking and formation, eventually building up a polymeric membrane [54]. Partial charges are updated to follow the charge-neutrality and force field assignments. Geometry optimization and 40 annealing cycles are performed for the generated cross-linked polymer, and the optimized cross-linked polymer membrane is used for subsequent calculations.

2.2. Hydration and desalination membrane model

The standard approach for the hydration model [55,56] is to directly fill water molecules into the PA membrane to match an experimental water content of 23 wt% [57], where water molecules are also artificially inserted into the inaccessible voids of PA membrane. Here an alternative is to drive the hydration process in equilibrium MD simulations using physical PA-water interaction. Before driving the hydration process, a 50 Å by 50 Å graphene sheet piston using its two-dimensional hexagonal lattice unit-cell at each end is placed to confine the reservoir. The left side, namely the feed reservoir, is 6 nm away from the PA membrane. The right side, namely permeate reservoir, is 3 nm away from the PA membrane. Then water molecules are randomly packed into the available volume field of the simulation box with a water density of 1.0 g cm^{-3}. In the end, the produced structure was equilibrated under the NVT ensemble long enough for hydration [40]. As shown in Fig. 1 (d), the desalination model is developed by adding the salt ions based on the hydration model. The salinity in the feed reservoir is close to that of typical brine water (~4 M) [58], and the permeate reservoir only contained pure water. Then a long enough simulation time is performed to equilibrate the altered structure under the NVT ensemble for the desalination model. Details of the MD simulations are shown in the next part.

2.3. Model systems for MD simulations

The focused PA RO membrane systems mainly consist of different DCs and MPD/TMC ratios. Seven models with the same MPD/TMC ratio of 3.0:2.0 but different DCs were prepared, including 40%, 50%, 60%, 70%, 80%, 90% and 96%. The number of the MPD and TMC monomers were 300 and 200, respectively, homologous with the MPD/TMC ratio of 3.0:2.0. The targeted DC is implemented by governing the percent of reactive atoms on monomers. As shown in Fig. 1(b), another four models with different MPD/TMC ratios were numerically generated, including 1.0:1.0, 1.0:4.0, 3.0:2.0, and 4.0:1.0. The numbers of MPD and TMC monomers were 250 and 250, 100 and 400, 300 and 200, and 400 and 100 in the main cells, which correspond to the MPD/TMC ratios 1.0:1.0, 1.0:4.0, 3.0:2.0, and 4.0:1.0, respectively. The main cell for all the different MPD/TMC ratios and DCs is a cubic unit cell with an approximate length of 50 Å. The unit cell size and total monomer numbers were employed according to a previous theoretical study on the MPD/TMC ratio of 1.0:1.0 [59]. These PA membrane models are used for performing the RO process by assembling water molecules, salt ions, and graphene sheet pistons. Besides, taking membrane with 90% DC and MPD/TMC ratio of 3.0:2.0 as an example, three independent models are conducted to eliminate the statistical randomness.

2.4. NEMD simulations for RO desalination through PA membrane

Setting up for all-atom MD simulations of water and salt ions transport through PA membrane is shown in Fig. 1(d), following our previous study [60]. The initial system is set as a cuboid box with 140 Å in the *z*-direction and 50 Å by 50 Å in the *x* and *y* directions. Two graphene sheets are used for pistons and are located at $z = 0$ and 140 Å. PA membrane with a thickness of 50 Å is initially placed at $z = 60$–110 Å. Water molecules, or water molecules and salt ions, are then packed into the simulation box. The number of water molecules is consistent with water density, 1.0 g cm^{-3}, and the number of salt ions is only packed into the feed reservoir ($0 < z < 60.0$ Å), which corresponds to a salinity of 40.0 g L^{-1}, close to the 38.6 g L^{-1} of typical brine water. Notably, a fraction of atoms (highlighted by blue) of the PA membrane located at the permeated side is randomly selected and fixed to mimic the attachment on a substrate (polysulfone support layer). This can ensure a more natural response of the PA membrane to match the pressure and flow conditions [44,61,62]. Studies have indicated that fixing some membrane atoms may slightly impact the transport flux but no impact on the transport mechanism [63]. Periodic boundary conditions are only applied in the *x* and *y* directions.

Any interatomic interactions involving water molecules, graphene, PA membrane, and salt ions are defined by polymer consistent force field (PCFF) [64–66]. PCFF is a second-generation force field and is parameterized for organic compounds, such as C, H, O, N, P, S, halogen atoms, and ions, which have been widely used to describe the cohesive energies, compressibilities, mechanical properties, elastic constants, and so on. Non-bonded interactions are characterized by both LJ and Coulomb potentials:

$$U_{\text{nonbonded}} = \varepsilon_{ij}\left[2\left(\frac{\sigma_{ij}}{r_{ij}}\right)^{9} - 3\left(\frac{\sigma_{ij}}{r_{ij}}\right)^{6}\right] + C\frac{q_i q_j}{\varepsilon r_{ij}} \quad (1)$$

where r_{ij} is the distance between atoms *i* and *j*, ε_{ij} represents the depth of the LJ potential well between atoms *i* and *j*, σ_{ij} represent the distance at which the LJ potential is the minimum between atoms *i* and *j*, and q_i and q_j are the partial charges on atoms *i* and *j*, respectively. *C* is a unit conversion factor and ε is a relative dielectric constant. The potential interactions between different atoms are calculated using the six-power combination rules [67]: $\varepsilon_{ij} = \sqrt{\varepsilon_i \varepsilon_j}\,(2r_{ii}^3 r_{jj}^3)/(r_{ii}^6 + r_{jj}^6)$ and $\sigma_{ij} = (\sigma_{ii}^6 + \sigma_{jj}^6)^{\frac{1}{6}}/2^{\frac{1}{6}}$. van der Waals and electrostatic interactions are truncated smoothly with a cutoff of 10.0 Å. Particle–particle particle–mesh

(PPPM) solver with a force tolerance of 10^{-4} is used to calculate the long-range electrostatic interactions.

Employing the Large-scale Atomic/Molecular Massively Parallel Simulator (LAMMPS) package [68], all MD simulations are performed using the velocity-Verlet algorithm's integration method and a time step of 1.0 fs. In the equilibrium stage, first, energy minimization is carried out on the entire system to achieve a stable initial configuration. Next, the atmospheric pressure of 0.1 MPa is imposed on the graphene sheets. A long simulation time of 20 ns is performed for MD simulation under the NVT ensemble at 300K, which ensures the solutions and PA membrane fully equilibrate to obtain the stable hydration or desalination membrane model. PA membrane performance indexes, such as density, membrane microstructure, and local structure, are analyzed during equilibrium simulation.

Concerning the non-equilibrium simulation of pure and brine water, 0.1 MPa (standard atmosphere) and an initial simulation time 2 ns are first exerted to the graphene sheets to allow the solutions and PA membrane to equilibrate under the NVT ensemble at 300 K fully. And then, a higher pressure ($\Delta P = 30$, 60, 90, 120, or 150 MPa) is applied to the left graphene piston on the feed side while keeping the right graphene piston at 0.1 MPa under the NVT ensemble at 300 K. Compared with the typical PA RO membrane processes, these higher pressures can facilitate the well-converged statistics within a reasonable time scale [69–71]. Besides, Gaussian velocity distribution is used for initializing the initial temperature-consistent of molecules, and a Nosé-Hoover thermostat [72,73] is employed to maintain the system at 300 K under the NVT ensemble. Simulations are carried out for 70 ns, and results are shown in **Section 3**. During these non-equilibrium simulations, performance metrics, such as water flux, membrane density, membrane microstructure, and water accessible volume distribution of the hydrated PA membranes, are calculated for a pure water system. Performance metrics such as water flux, rejection of salt ions, density distribution, and dynamic behaviors of salt ions are also monitored for the brine water system.

3. Results and discussion

3.1. Atomic-scale structural clarification for PA membrane with different DCs

To characterize the effect of DC on PA membrane structure, we analyze the membrane composition, density of the hydrated PA membrane as well as its two components (water and PA membrane), and pore size distribution after membrane models are sufficiently equilibrated and hydrated. Table 1 shows the atomic compositions in molar percentage, DCs, and densities of PA membrane with the MPD/TMC ratio of 3.0:2.0 at different DCs. As the DC increases from 40.07% to 96.26%, the percentage composition of carbon (C), nitrogen (N), oxygen (O in carbonyl group) also increase from 62.756% to 74.132%, 11.596%–12.407%, and 4.658%–11.973%, respectively. However, the percentage composition of the carboxyl group (-COOH) decreases from 20.990% to 1.489%. This is because more acyl carbon and amino nitrogen atoms induce the crosslinking reaction (Fig. 1(c)), accompanied by decreasing –COOH groups and the increasing carbonyl groups (-C═O). Compared with the membrane having 96.26% DC and MPD/TMC ratio of 3.0:2.0, results are overall consistent with the experimental measurements using Rutherford backscattering spectrometry (RBS) by Coronell et al. [20]. Densities for different DC membranes in Table 1 are also both in good agreement with the experimental value of 1.22–1.28 g cm^{-3} for PA thin films [26] and the other computing result of 1.25 g cm^{-3} [43,45,74]. Thus, the compositions in Table 1 can provide a guidance to design the PA membrane by tuning the oxygen content and DC at the molecular level.

For the local density, the simulation box is separated into serval slabs with a thickness of 2 Å along the z-direction. The local density of water, PA membrane, and the hydrated PA membrane are calculated based on the local slab volume. Fig. 2(a) shows the local density profiles of the hydrated PA membrane as well as the two components, water and PA membrane. Density profiles show that membranes are roughly divided into three regions. First is the confined layer, corresponding to the densest membrane, i.e., between $z = 80$–115 Å. Second is the transition layer, or the interfacial layer between the membrane and water reservoirs, corresponding to low-density and looser membrane structures, i.e., between $z = 69$–80 Å, and $z = 115$–126 Å. The last is bulk water layer, i.e., between $z = 8$–69 Å, and $z = 126$–157 Å. Notably, the transition layer is caused by the cross-linking reaction, which is different from the swelling caused by hydration in systems of linear polymer chains [75]. Water density is about 0.99 g cm^{-3} in the bulk water layer, which is in well accordance with the bulk water density at room temperature [76]. An average density of 1.32 g cm^{-3} (0.27 g cm^{-3} for water and 1.05 g cm^{-3} for PA membrane) is identified for the hydrated PA membrane within the confined layer, which is in line with the experimental measurement of 1.30 ± 0.1 g cm^{-3} for the commercial FT-30 membrane having a water content of 23 wt% [77–79]. Besides, we observe that as the DC decreases, more unreacted MPD or TMC monomers break away from the membrane and reside in the bulk water, consistent with previous experimental observations [80–82].

In addition to membrane composition and density, MD simulations also provide a direct way to analyze the membrane pore size at the atomic scale. The pore size is quantified by PSD, capturing PA membrane's microstructure. PSD is calculated by using PoreBlazer [83] with a probe diameter, 2.8 Å (Coulombic diameter of one water molecule), which is a reasonable size estimation for water molecule [84,85] interacting with polar atoms. Based on the equilibrium simulation over 20 ns, the last six configurations are chosen to analyze the PSD of PA membrane. The final PSD curve is obtained by averaging the six values. PSD is calculated from the confined region and half of the transition region in the membrane. Fig. 2(b) shows PSD curves for the PA membrane with seven different DCs. Videos of the membrane microstructure at 0.1 MPa over 20 ns are available as supplementary material (**V1–V4**) to display the pore space distribution more clearly. Results show that PA membranes with different DCs show a pronounced difference in PSD curves with pores ranging from 2.5–20 Å, and the pore size is more homogeneous with the increasing DC as the cross-linking reaction can arise through the whole membrane. Importantly, PSD curves tend to move towards the left with the increasing DC. As the DC increases from

Table 1
Atomic composition, DCs, and density of PA RO membranes formed with different DC. For comparison, the experimental result is also displayed [20,31].

MPD/TMC Ratio		Atomic Composition				DCs (%)	Density (g cm^{-3})
		C%	N%	O%	COOH%		
Simulation	3.0:2.0	62.76	11.60	4.66	20.99	40.07	1.24
		64.70	11.74	5.91	17.66	50.21	1.25
		66.65	11.87	7.16	14.31	60.18	1.24
		68.66	12.02	8.45	10.88	70.16	1.25
		70.71	12.16	9.771	7.36	80.13	1.23
		72.77	12.31	11.10	3.82	89.94	1.23
		74.13	12.41	11.97	1.49	96.26	1.22
Experiment	3.9:1.0	71.60–74.20	12.40–13.10	13.00–14.20	0.41–0.71	94.10–96.20	1.22–1.28

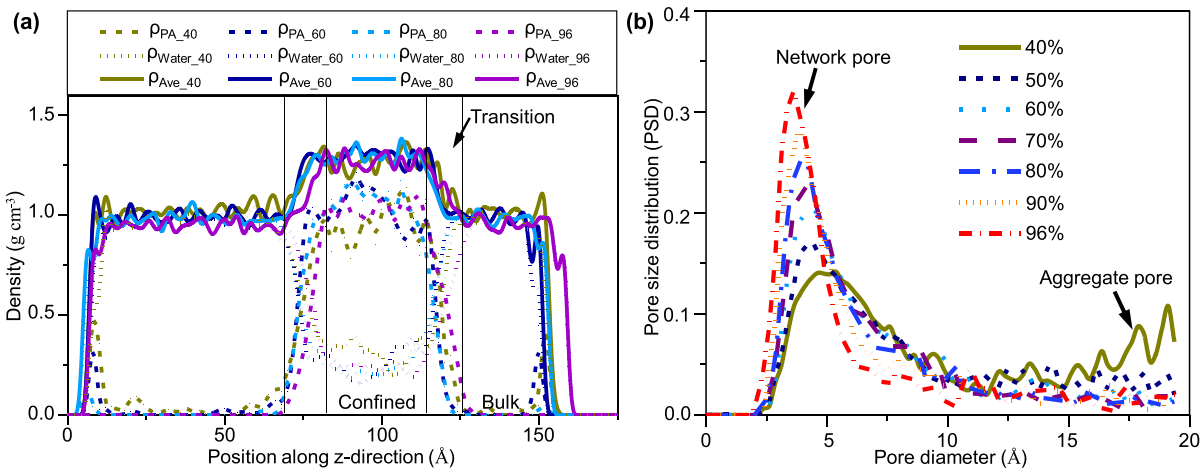

Fig. 2. (a) Axial local density profiles along z-direction for the hydrated PA membranes with different DC, and its two components (water and PA membrane) in pure water. The dashed line is the PA membrane, the dotted line is water and the solid line is the hydrated PA membrane. For clarity, only four DCs: 40% (green), 60% (dark blue), 80% (blue) and 96% (purple) are displayed. (b) Pore size distribution for PA RO membranes with DC ranging from 40% to 96%. (For interpretation of the references to color in this figure legend, the reader is referred to the Web version of this article.)

40% to 96%, peaks in PSD curves show a significant shift from 0.14 to 0.32. Meanwhile, pore sizes corresponding to the peaks have an evident decrease from 4.625 to 3.625 Å, which shows a downward trend for the formed network pores but are still larger than the diameter of the water molecule. Besides, the PA membrane has more pores with greater diameters when DC is below 60%, which reveals looser geometric characteristics. The increased large pores may indicate the presence of aggregate pores, which is in virtue of the open spaces existing in between polymer aggregates [86]. Similarly, PA membrane with DC above 60% only has network pores, corresponding to more pores with smaller diameters and denser geometric features. These findings in Fig. 2(b) indicate that PA membrane pore size can be tuned by governing the DC.

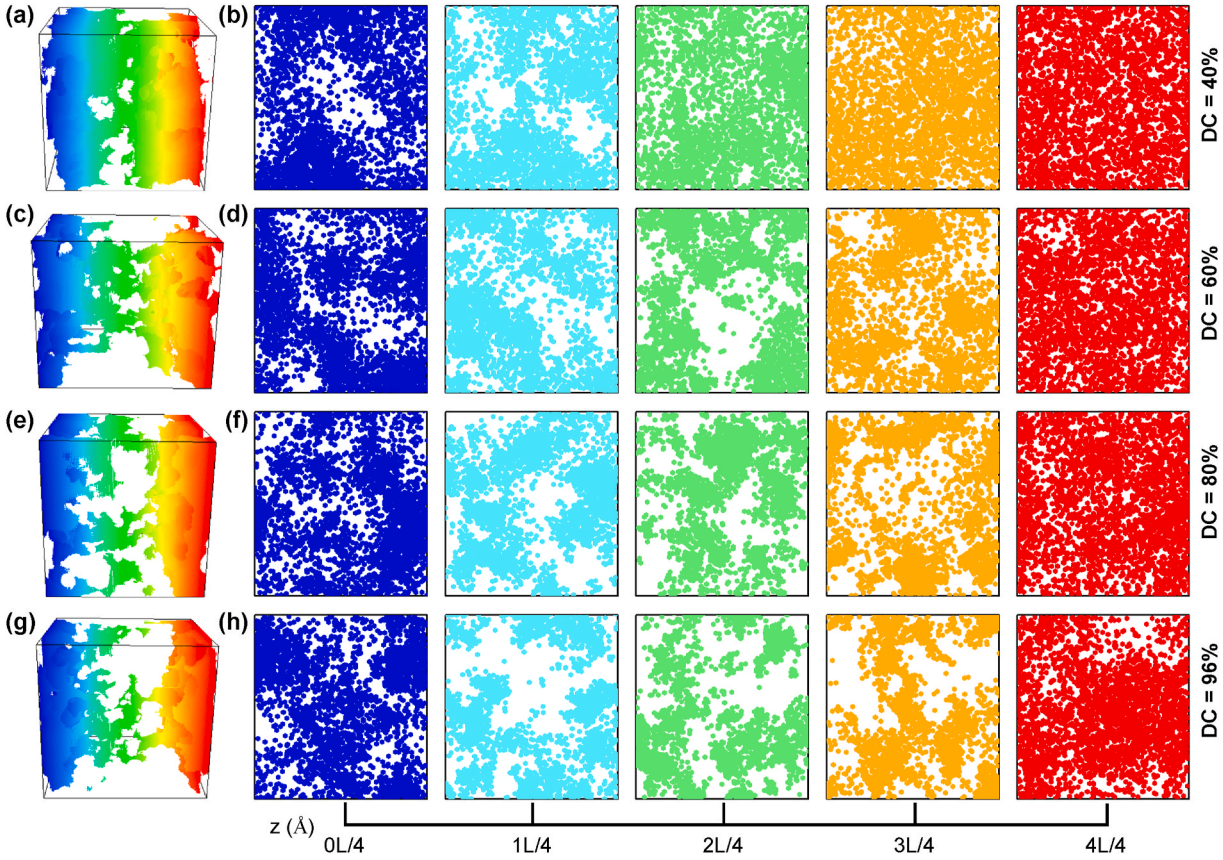

Fig. 3. The percolated water-accessible free volume distribution for the hydrated PA membranes with DC of (a) 40%, (c) 60%, (e) 80% and (g) 96% over 70ns. Each color represents a 1.0 Å thick plane at a different depth along z-direction. The accumulated water-accessible free space over 70 ns for PA membrane with DC of (b) 40%, (d) 60%, (f) 80% and (h) 96% at z = 0L/4 Å, 1L/4 Å, 2L/4 Å, 3L/4 Å and 4L/4 Å. The color denotes the depth in the z direction. (For interpretation of the references to color in this figure legend, the reader is referred to the Web version of this article.)

Supplementary video related to this article can be found at https://doi.org/10.1016/j.memsci.2022.120731

Additionally, we also evaluate the water diffusivity through the membranes using the water molecules' mean square displacements (MSDs) [87]. As shown in Figs. S1(a–f), for each membrane, water diffusion in the bulk water region is slightly higher than that in the transition region, but both of them are higher than that in the confined region. Increasing DCs don't affect water diffusivity in the bulk water region and transition region, but they result in a slight decrease in the confined region.

3.2. Effect of DC on dynamic behaviors of the permeated water molecules

Membrane with different DCs can lead to different pore sizes, confirmed by the PSD curves in Fig. 2(b), and can be further characterized in the matter of the size and connectivity of the accessible water space, or free volume space within the membrane. These different pore sizes may dramatically affect water transport benefits. Membrane pore structure is then studied by analyzing the percolated water-accessible volume space by using a probe diameter of 2.8 Å (Coulombic diameter of one water molecule). Fig. 3(a, c, e, g) shows the percolated water-accessible free volume distribution for the hydrated PA membrane with different DCs at 150 MPa over 70 ns. Here, in clarity, we only display the membrane having the DC of 40%, 60%, 80%, and 96%. A video of the percolated water-accessible volume at 150 MPa viewed as shown in Fig. 3(a, c, e, g) over 70 ns is available as supplementary material (**V5–V8**) to more clearly demonstrate the size and connectivity of the accessible water space. The gradient colors (from blue to red) represent the membrane thickness along z-direction. The colored area shows the percolated volume spaces that allow water molecules to pass through the membrane. The "pore" used in this study is not the pore flow model's pore features but the water-accessible space in the membrane. Results indicate that the total percolated free volume is noticeable different, when membrane DC changes from 40% to 96%. The unconnected percolated water-accessible volume decreases as the DC decreases, and more connected percolated water-accessible volume space is visible.

Supplementary video related to this article can be found at https://doi.org/10.1016/j.memsci.2022.120731

To further demonstrate the relevance between water transport and the percolated water-accessible free volume, we analyze the dynamic pore dimensions when water molecules traverse through the membrane within the percolated free volume. The dynamic pore dimensions are caused as a result of thermal vibrations and collisions between membranes and water molecules, which can be described by an accumulated free volume over a long time. Fig. 3(b, d, f, h) shows that the percolated water-accessible free volume accumulated over 70 ns within the membrane region at z = 0L/4 Å, 1L/4 Å, 2L/4 Å, 3L/4 Å, and 4L/4 Å. The accumulated free volume percolated in the z-direction is a significant difference for membrane having different DCs at the same position and the same DC at different positions. We find that the membrane with a lower DC has more accumulated free volume and can allow more water molecules to pass through the membrane.

Moreover, on one side, other previous studies indicated that the percolated free volume is directly related to the permeability coefficient, K, which is used to describe the water transport passing through the membrane [55]. The low DC membrane has a more percolated free volume for water transport. On the other side, by observing Fig. 3(a–h), water molecules passing through the membrane are more likely through both the continuum channels and the temporary on-and-off channels jumping from one pore to another for membranes having the lower DC. While it is more pronounced in the temporary on-and-off channels jumping from one cavity to another for membranes with the higher DC. These findings also verify a recent study [45] that water transport for the highly cross-linked membrane is solution-diffusion rather than the pore-flow model.

3.3. Pressure dependence of water desalination for membranes with different DCs

Before simulation with brine water, we first explore the pure water transport through PA membrane with the DC ranging from 40% to 96% at different pressure (from 30 MPa to 150 MPa, Fig. S2(a-b)). Results show that, besides 40% DC at both 120 MPa and 150 MPa and 50% DC at 150 MPa, water flux is almost linearly increased with the increasing pressure for membrane with the same DC. However, water flux decreases with the increasing DCs under the same pressure. In addition, the calculated water flux is mostly linearly increasing with pressure and intersects the flux axis at the origin due to the zero osmotic pressure, which also agrees with the ideal pure water flux-pressure curve. In contrast, experiments revealed that the macroscale water flux at the pressure of 4.1 MPa is between 2.4×10^{-5} m s^{-1} and 9.8×10^{-5} m s^{-1} for a typical commercial RO membrane [88]. Water flux is expressed as, $J = -K(\Delta P - \Delta P_0)/L$, where K is the permeability coefficient, L is the membrane thickness, K/L is the permability and ΔP is the pressure difference applied on the membrane, and ΔP_0 is the osmotic pressure. Water flux for membrane with the 96% DC and 50 Å thickness at 150 MPa should be proportionally in the range of 0.0364–0.147 m s^{-1}, and its macroscale flux corresponding to water molecule number should be in the range of 1.41–5.73 nm^{-2} ns^{-1}. The water flux for membrane with 96% DC at 150 MPa, is calculated as 2.55 nm^{-2} ns^{-1} (Fig. S2(b)), which agrees with the macroscale flux range well. Besides, similar comparisons with other experiments and simulation for the macroscale water flux also give a water molecule flux of 1.3–6.0 nm^{-2} ns^{-1} [86,89], and 1.7 to 6.9 nm^{-2} ns^{-1} [55] changed into the same condition as this study, respectively, which are also consistent with the calculated water molecule flux here. Therefore, the calculated water flux (Fig. S2(b)) in pure water demonstrates that our simulation model and timescale are reasonable.

To evaluate the pressure-driven transport with brine water, we monitor the number of the permeated water molecules, water flux, rejection rate of salt ions, salt ions dynamics behavior, density, and PSD for membrane with different DCs at high pressure. Fig. 4(a) displays that water transported through PA membrane with the DC changing from 40% to 96% at 30–150 MPa with the brine water, in the matter of the number of water molecules passing through the membrane as a function of time. Membranes have 40% DC at 120 MPa and 150 MPa, and 50% DC at 150 MPa are destroyed. In addition to this, after about 5 ns, as expected, water molecules permeate almost linearly with time. There was a rapid rise of the permeated numbers at the beginning 5 ns along with a thickness reduction of around 5–10%, indicating that some water molecules are squeezed out into the permeated side along with the compaction of PA membranes. Analogous situations are also observed for the other membranes. In addition, the permeated water molecules increase with increasing pressure at the same DC and show a decreasing trend as the increasing DC at the same pressure. Based on the slope of the linear regime in Fig. 4(a) and the cross-sectional area of the membrane, we calculate the water flux, in terms of the number of water molecules passing through the membrane with different DC per unit area per unit time as a function of pressure, shown in Fig. 4(b). Water flux has a positive association with the increasing pressure for membrane with the same DC and a negative correlation with increasing DC for membrane supporting the same pressure, both of which are similar to that of pure water transport (Fig. S2(a-b)). Through a comparative analysis of Fig. 4 (a-b) and Fig. S2(a-b), for the membrane having the same DC under same applied pressure, both the number of water molecules passing through the membrane and water flux with brine water is relatively smaller than that with pure water, which indicate that salt ions can hinder water molecules from passing through the PA membrane.

Next, our interest is the salt ions transport within the membrane. Fig. 5 shows the rejection ratio of salt ions as a function of pressure for membrane with the DC ranging from 40%~96% at different pressure (from 30 MPa to 150 MPa). Rejection ratio is defined as the percentage

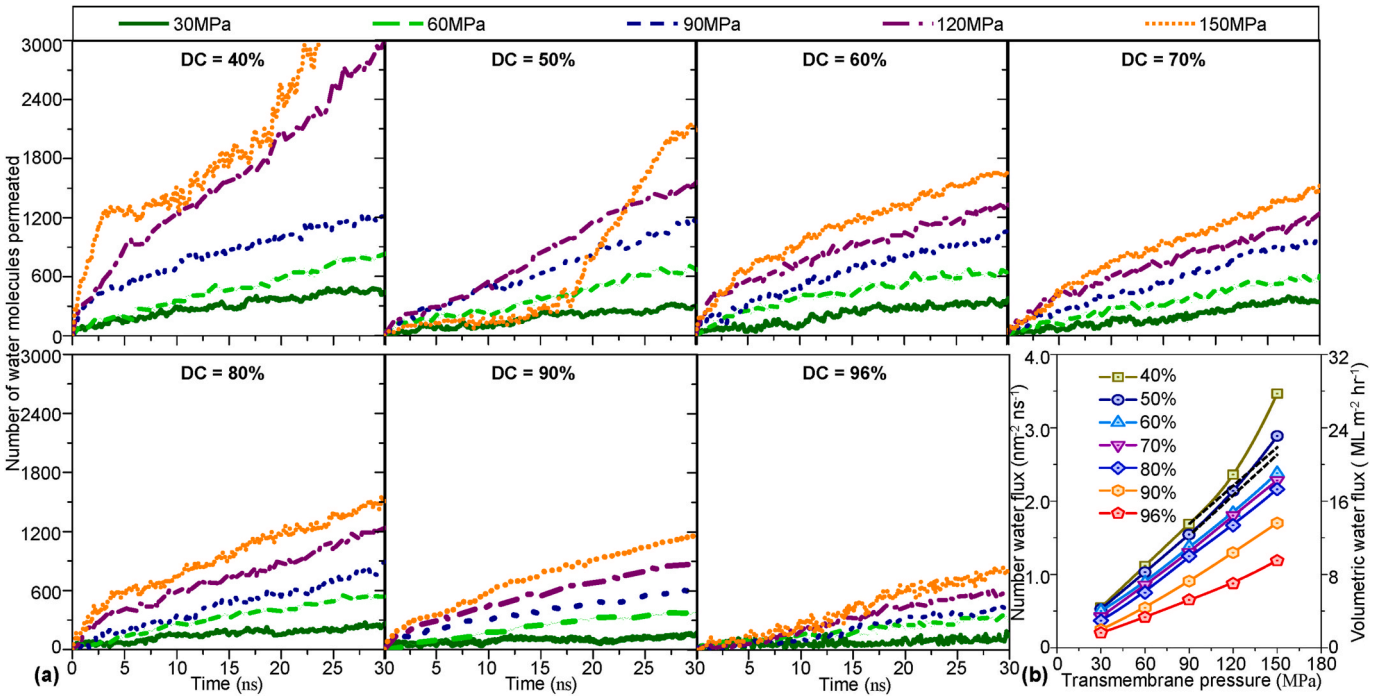

Fig. 4. Brine water transport at high pressures (from 30 to 150 MPa) through PA RO membranes with DC ranging from 40% to 96%. (a) Number of water molecules transported through the membrane as a function of simulation time at high pressure. (b) Water flux as a function of pressure for PA RO membrane with different DCs.

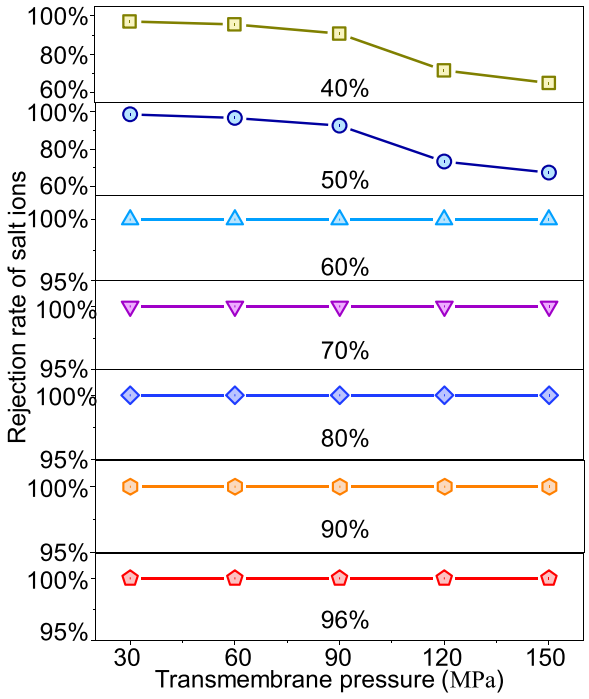

Fig. 5. Rejection of salt ions as a function of pressure for PA RO membranes with different DCs (from 40% to 96%).

of the number of salt ions not passing through the membrane to the total salt ions number. Results show that when DC is larger than or equal to 60%, the membrane can entirely reject salt ions at any pressure within our MD simulation timescale. Conversely, some salt ions can pass through the PA membrane, and the rejection rate of salt ions decreases with the increasing pressure, especially in the high-pressure regime. These findings can be further demonstrated by density profiles of salt ions (Na^+ and Cl^-, Fig. S3(a-n)) along z-direction before the *trans*-membrane pressure is applied (0 ns), and 70 ns after a 150 MPa pressure is applied to the left graphene. More than that, we examine the dynamics of essential salt ions (Fig. S4(a-w)) for membrane with different DCs at 150 MPa. When DC is above 60%, all salt ions usually spend most of their time hovering at the bulk water and stay at membrane-water interfacial region for a while. Besides, when DC drops to 60%, a few salt ions are penetrated into the dense membrane region, holding at a specific position and still not passing through the membrane. However, some salt ions can pass through the membrane having a DC below 60% following the continuum-like water channels (Fig. 3). Beyond that, we also monitor the dynamics of some key water molecules (Figs. S5(a–w)) for PA membranes with different DCs at 150 MPa. Water transport for highly cross-linked membranes mainly depends on the jumping transport at high pressure, and transport time through the membrane increases with the increasing DC.

Furthermore, we explore the structural characteristics of the PA membrane with different DCs at high pressure. Fig. 6 plots the PSD as a function of pore diameter for membrane with different DCs at different pressures. Interestingly, we observed that when DC is above 50%, the applied pressure, especially in the high-pressure regime, causes a rapid contraction of the free volume and membrane thickness, which agrees with the recent experimental investigation on the thin film composite RO membrane [90]. Besides, by analyzing the density profiles of the membrane with the DC ranging from 40% to 96% at different pressures (from 30 MPa to 150 MPa, Fig. S6), it can be found that more unreacted monomers are gradually driven out of the membrane surface and move into the bulk water as either the DC decreases at the same pressure or the pressure increases at the same DC. In particular, PA membranes with 40% and 50% DCs exhibit the inhomogeneous structural features.

3.4. *Effect of MPD/TMC ratio on PA membrane microstructure*

To illustrate the effect of MPD/TMC ratio on membrane structure at atomic level, four MPD/TMC ratios, 1.0:1.0, 1.0:4.0, 3.0:2.0 and 4.0:1.0, are used for membrane models. Membrane composition, the density of the hydrated membranes and its two components (water and PA

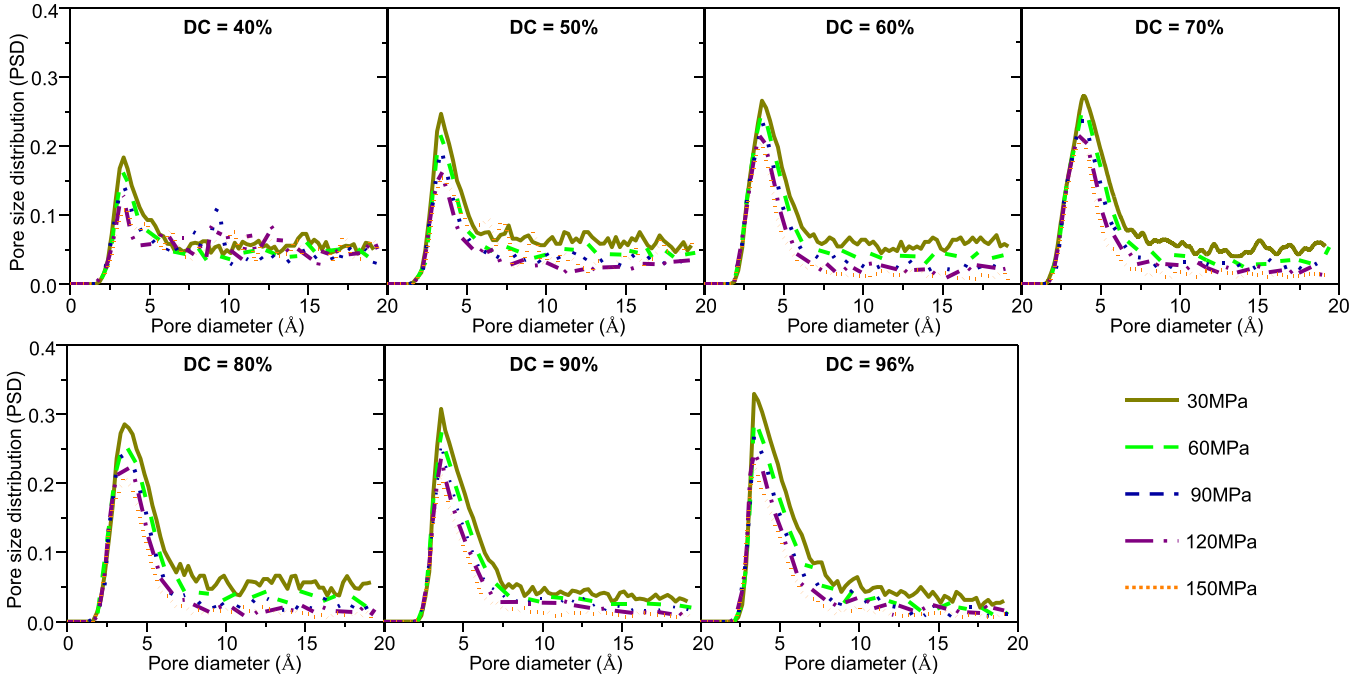

Fig. 6. Pore size distribution for PA RO membranes with the DC ranging from 40% to 96%, under different pressures (from 30 MPa to 150 MPa).

membrane), the spatial distribution of benzene rings, and PSD, are used to evaluate membranes' structural properties. Table 2 shows the DCs, density, composition ratios of the C, O, N, and –COOH group for PA membrane with four MPD/TMC ratios, 1.0:1.0, 1.0:4.0, 3.0:2.0, and 4.0:1.0, and the corresponding experimental measurements. The total number of MPD and TMC monomers is 500 for each of the four MPD/TMC ratios. As the number of MPD increases from 1.0:4.0 to 1.0:1.0 to 3.0:2.0 to 4.0:1.0, the percentage composition of C and N increase, the –COOH groups decrease, and the O content first increases and then decreases, which is due to both the different monomer numbers and reactive sites between MPD and TMC monomers. In addition, composition ratios for membrane with the MPD/TMC ratio 3.0:2.0 are well agreement with the corresponding measurements by RBS due to the similar DC [20]. MPD/TMC ratio of 1.0:4.0 has the lowest DC due to the least MPD monomers leading to the least reactive sites. Also, although the MPD/TMC ratio of 4.0:1.0 has the least TMC monomers, DC is higher than that of 1.0:4.0 as a result of more reactive sites consisting of TMC monomers. A higher DC can be achieved for MPD/TMC ratios of 3.0:2.0 and 1.0:1.0 due to the comparable reactive sites existing in MPD and TMC monomers. Densities for membranes with MPD/TMC ratio of 1.0:1.0 and 3.0:2.0 have no obvious difference and is in the range of 1.16–1.30 g cm^{-3} in Table 2, which agrees with both the measurements of 1.22–1.28 g cm^{-3} and other MD simulation results of 1.25 g cm^{-3} [34,43,91]. However, due to more unreacted TMC monomers having the higher density of 1.487 g cm^{-3}, the PA membrane with an MPD/TMC ratio of 1.0:4.0 has a higher density. Similarly, more unreactive MPD monomers with the lower density of 1.14 g cm^{-3} lead to a lower density for the PA membrane with MPD/TMC ratio of 4.0:1.0.

In addition, local membrane structure is characterized by the interactions between residual benzene groups. Studies have shown that the bonded and non-bonded interactions that are π-π stacking constraining the interactions between benzene groups [92]. To describe the stacking modes of benzenes for PA membranes with different MPD/TMC ratios, the order parameter [93,94], $S(r)$, is first investigated. $S(r)$ is described by $S(r) = <(3\cos^2(\theta(r)) - 1)/2>$, where r is the radial distance, $\theta(r)$ is the angle defined by the normal vectors of benzene rings at r (see Fig. 7(a)). Physically, S(r) close to 1 corresponds to the wholly ordered packing, S(r) close to −0.5 represents T-shaped packing, and S(r) close to 0 denotes a random structure. The relative local density of benzene rings is described by the radial distribution $G(r)$, expressed as $G(r) = \rho(r)/\rho_{bulk}$, where $\rho(r)$ is the benzene density at the location of r, and ρ_{bulk} is the bulk density. G(r) close to 0 suggests the absence of benzene rings. When r is large enough, G(r) is close to 1. Fig. 7(b-c) respectively show the order parameter, $S(r)$, and relative local density, $G(r)$, of benzene rings as a function of the radial distance for PA membrane with four MPD/TMC ratios. The nearest radial distance is about 6 Å for MPD/TMC ratio 1.0:1.0 and 4.0:1.0, and 4 Å for MPD/TMC ratio 1.0:4.0 and 3.0:2.0. Within the radial distance of 16 Å, the order parameters, $S(r)$, are approximately three types, including −0.3, 0 and 0.3 (1.0:1.0), −0.4, 0 and 0.6 (1.0:4.0), −0.4, 0 and 0.6 (3.0:2.0), −0.2, 0 and 0.2 (4.0:1.0) for membranes with the four MPD/TMC ratios, which indicate that MPD/TMC ratio can determine the spatial arrangement

Table 2
Atomic composition, DCs, and density of PA RO membranes fabricated with four MPD/TMC ratios, 1.0:1.0, 1.0:4.0, 3.0:2.0 and 4.0:1.0. For comparison, the experimental measurement is also displayed [20,31].

MPD/TMC Ratio		Atomic Composition				DCs (%)		Density (g cm^{-3})
		C%	N%	O%	COOH%	Simulation	Ideal	
Simulation	1.0:1.0	64.98	9.99	9.97	15.05	100.00	100.00	1.24
	1.0:4.0	50.00	2.94	2.94	44.12	100.00	100.00	1.28
	3.0:2.0	69.86	13.70	12.33	4.11	90.00	100.00	1.26
	4.0:1.0	73.17	19.51	7.32	0.00	100.00	100.00	1.17
Experiment	3.9:1.0	71.60–74.20	12.40–13.10	13.00–14.20	0.41–0.71	94.10–96.20	100.00	1.22–1.28

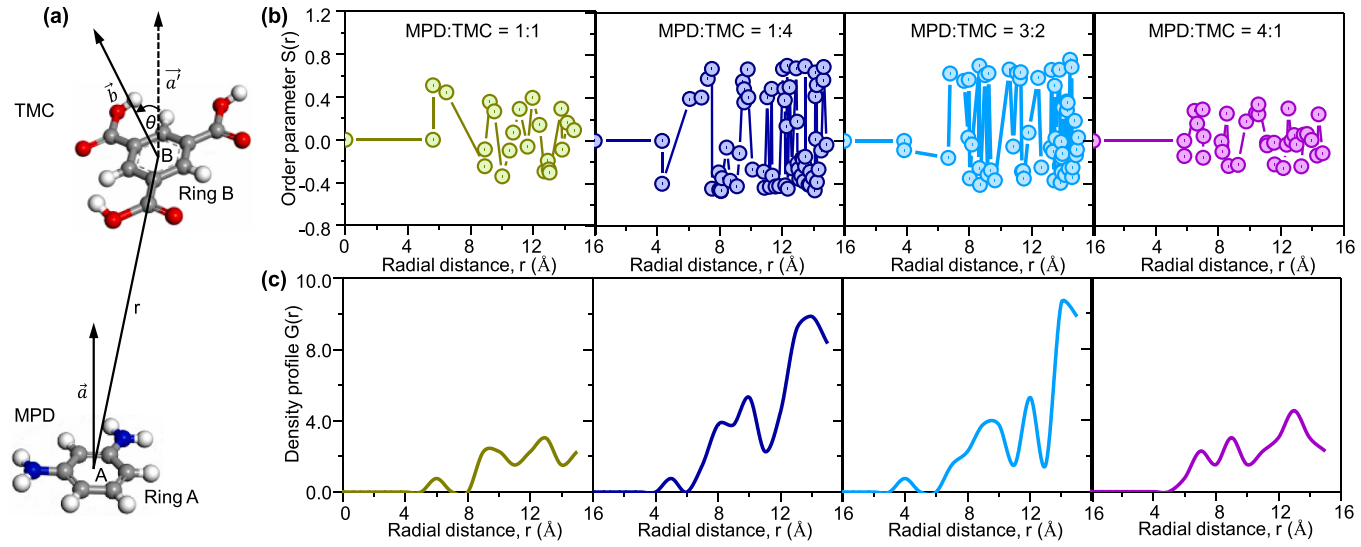

Fig. 7. (a) Definition for the local structure of PA membrane. (b) Benzene rings' order parameter, S(r), and (c) density profile, G(r), as a function of radial distance, r, for PA RO membrane with four MPD/TMC ratios, 1.0:1.0, 1.0:4.0, 3.0:2.0, and 4.0:1.0.

between MPD and TMC monomers, and leads to the diverse membrane structures. Meanwhile, considering the density profile in Fig. 7(c) and Fig. S7, the membranes with the four MPD/TMC ratios have an obvious difference in benzene rings density, and return to 1 when the radial distance is larger enough. Membranes with the MPD/TMC ratio of 1.0:4.0 and 3.0:2.0 have a higher density of benzene than that of 1.0:1.0 and 4.0:1.0. The peak densities of benzene rings along the radial distance are at 6 Å, 9 Å and 13 Å (1.0:1.0), at 5 Å, 8 Å, 10 Å and 14 Å (1.0:4.0), at 4 Å, 10 Å, 12 Å and 14 Å (3.0:2.0), and at 7 Å, 9 Å and 13 Å (4.0:1.0). Notably, factoring in the order parameter and density at the same radial distance, it can be found that the membranes with different MPD/TMC ratios exhibit different local structural properties.

Next, the local density profiles of the hydrated PA membrane and its two components (water and PA membrane) are shown in Fig. 8(a). Three regions are identified: the confined layer having the dense membrane, the transition layer with loose structures, and the bulk water region. Water density within the bulk water region is about 0.99 g cm^{-3} for membrane with each MPD/TMC ratio, matching the bulk density of water well at room temperature. An averaged density of 1.33 g cm^{-3} (0.25 g cm^{-3} for water and 1.08 g cm^{-3} for PA membrane) is identified for the hydrated membrane with MPD/TMC ratio of 1.0:1.0, 3.0:2.0 and 4.0:1.0 within the confined layer, which is close to the experimental results of 1.30 ± 0.1 g cm^{-3} for commercial FT-30 membrane [77–79]. However, the hydrated PA membrane with an MPD/TMC ratio of 1.0:4.0 has a slightly larger averaged density of 1.39 g cm^{-3} (0.21 g cm^{-3} for water and 1.18 g cm^{-3} for PA membrane) due to the insufficient MPD monomers, leading to much more unreactive TMC monomers. Besides, some unreactive MPD or TMC monomers are driven out the membrane surface and reside into the bulk water layer for the PA membrane with an MPD/TMC ratio of 4.0:1.0. Correspondingly, the membrane with an MPD/TMC ratio of 4.0:1.0 shows a looser structure than the other three MPD/TMC ratios.

We further analyze the pore size at the atomic scale to grasp the microstructure for PA membranes with different MPD/TMC ratios employing PSD. Fig. 8(b) shows the averaged PSD curves for PA membrane with four MPD/TMC ratios, 1.0:1.0, 1.0:4.0, 3.0:2.0 and 4.0:1.0.

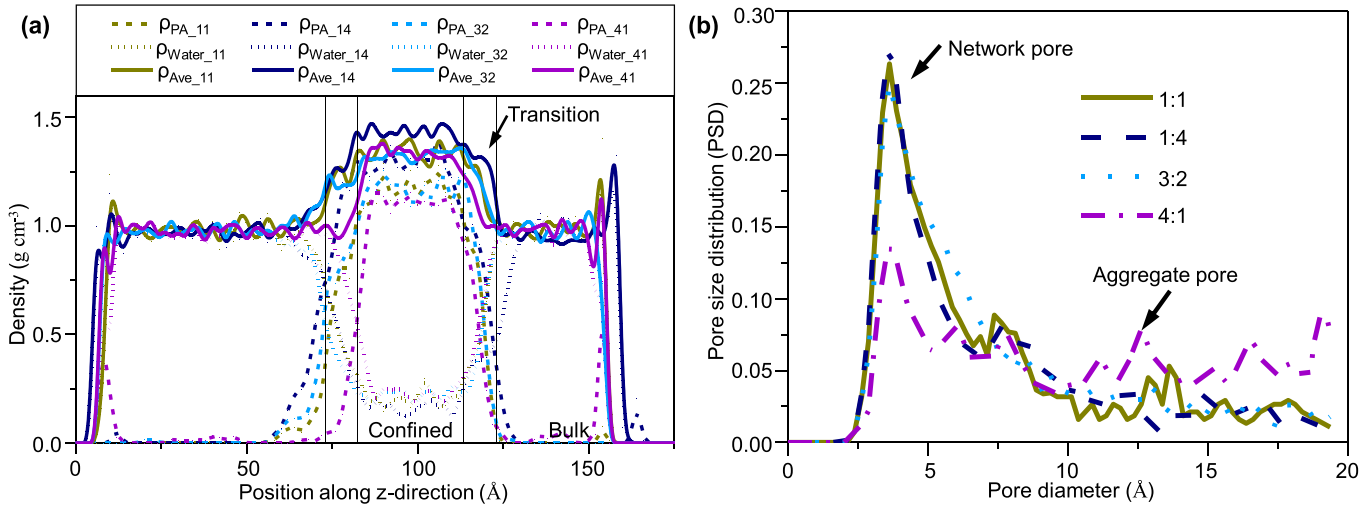

Fig. 8. (a) Axial local density profiles along z-direction for the hydrated PA membranes with four MPD/TMC ratios, 1.0:1.0, 1.0:4.0, 3.0:2.0 and 4.0:1.0 in pure water. The dashed line is the PA membrane, the dotted line is water, and the solid line is the hydrated PA membrane. (b) Pore size distribution for PA RO membranes with the four MPD/TMC ratios.

Videos of the microstructure at 0.1 MPa over 20 ns are available as supplementary material (**V9–V12**) to display the pore distribution more clearly. PSD curves remarkedly vary with different MPD/TMC ratios. When MPD/TMC ratios change from 1.0:4.0 to 1.0:1.0 to 3.0:2.0 to 4.0:1.0, PSD shows a right shift, and the size of the formed network pores keep unchanged, about 3.625 Å, and is larger than the water molecule diameter, 2.8 Å. Besides, the aggregate pores are identified for the membranes with different MPD/TMC ratios. Particularly, the membrane with the MPD/TMC ratio of 4.0:1.0 has more large pores, which presents a looser geometric feature. In addition, the PSD for membrane with an MPD/TMC ratio of 4.0:1.0 is more heterogeneous. This is because the membrane with an MPD/TMC ratio of 4.0:1.0 has insufficient TMC monomers leading to more redundant MPD monomers. For membranes with MPD/TMC ratios of 1.0:4.0 and 1.0:1.0, all MPD monomers are reacted, and some superfluous TMC monomers are scattered in PA membranes. The –COOH groups of TMC monomers can form hydrogen bonds with water molecules, –COOH groups of other TMC monomers, or the –C═O group in the amine group. These hydrogen bonds can strengthen the structural integrity of membranes and keep their pore distribution stable. Membrane with MPD/TMC ratio of 3.0:2.0 has the equivalent cross-linking sites for MPD and TMC monomers, which can scatter through the whole membrane and lead to a more homogeneous pore size. These findings indicate MPD/TMC ratios can govern membrane pore size, and the relationship between MPD/TMC ratios and pore size can be applied to tune and design membrane's microstructure.

Supplementary video related to this article can be found at https://doi.org/10.1016/j.memsci.2022.120731

Similarly, we further analyze water molecules' MSD (Fig. S8 (1-d)) to study the diffusivity through the membranes. Results indicate that membranes with different MPD/TMC ratios show similar water diffusivity trends. The diffusivity is slowest in the confined region, followed by the transition and bulk water regions. MPD/TMC ratios do not seem to influence water diffusion in the transition and bulk water regions. However, in the confined region, the membrane with an MPD/TMC ratio of 4:1 has the highest water diffusivity, followed by 3:2, 1:1, and 1:4. These findings indicate that different MPD/TMC ratios can also affect the water diffusivity in the PA membranes.

3.5. *Effect of MPD/TMC ratio on dynamic behaviors of the transported water molecules*

Different MPD/TMC ratios can lead to different pore size, reflected by different PSD curves in Fig. 8(b). Pore size and connectivity of the water-accessible space, or the free volume space within the membrane, can further characterize the dynamic behavior of water transport. Different pore sizes and connectivity can significantly affect the efficiency of water transport. To evaluate the effect of MPD/TMC ratio on water transport, employing a probe diameter of 2.8 Å, the percolated water-accessible free volume for membranes with different MPD/TMC ratios in the hydrated state at 150 MPa over 30 ns are shown in Fig. 9(a, c, e, g), respectively. Video of the percolated water-accessible space at 150 MPa viewed as shown in Fig. 9(a, c, e, g) over 30 ns are available as supplementary material (**V13–V16**) to reveal the size and connectivity of the water-accessible space more clearly. Gradient color changing from blue to red denotes the membrane thickness along z-direction, and the colored region represents the percolated volume spaces for water molecules passing through the membrane. Obviously, membrane with MPD/TMC ratio of 4.0:1.0 has the largest free volume space, followed by

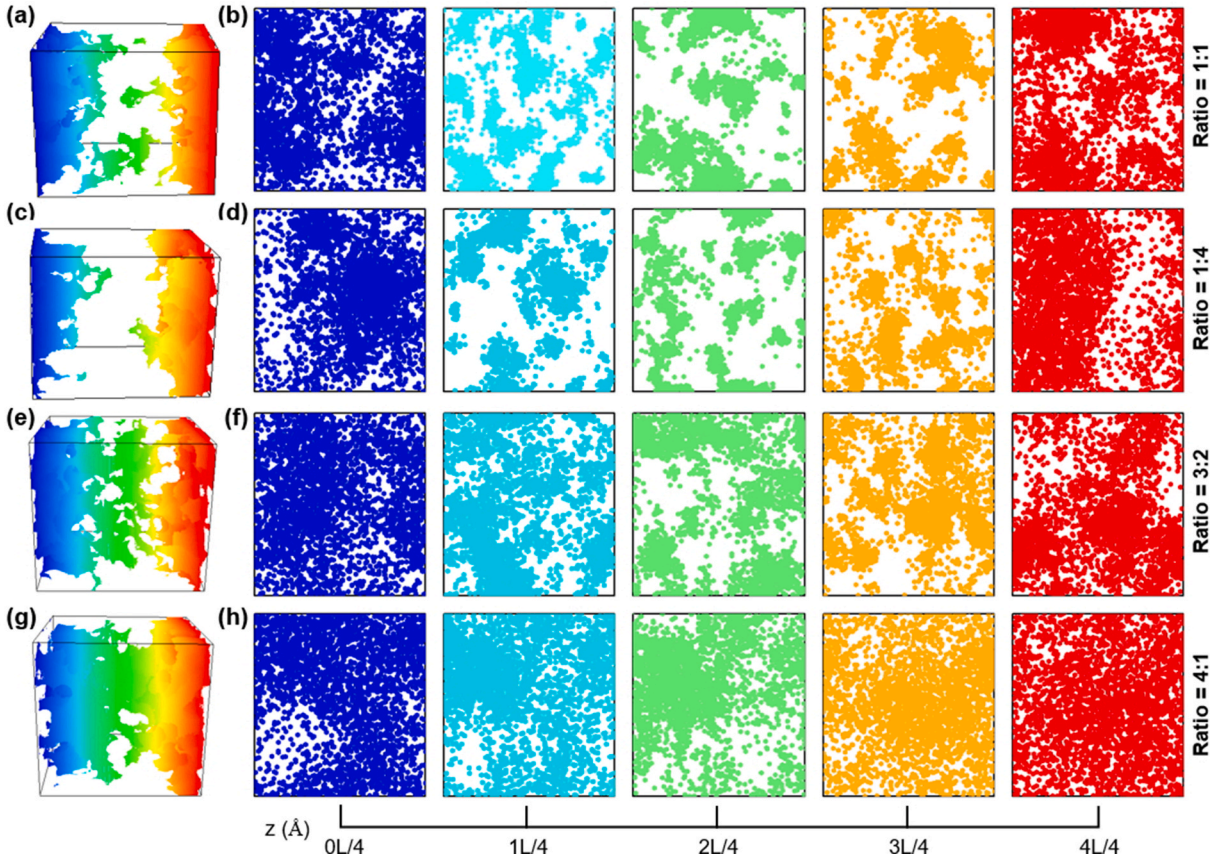

Fig. 9. The percolated water-accessible free volume distribution for the hydrated PA membranes with MPD/TMC ratios of (a) 1.0:1.0, (c) 1.0:4.0, (e) 3.0:2.0 and (g) 4.0:1.0 over 30 ns. Each color represents a 1.0 Å thick plane at a different depth along z-direction. The accumulated water-accessible free space over 30ns for PA membrane with MPD/TMC ratios of (b) 1.0:1.0, (d) 1.0:4.0, (f) 3.0:2.0 and (h) 4.0:1.0 at x = 0L/4 Å, 1L/4 Å, 2L/4 Å, 3L/4 Å and 4L/4 Å. The color displays the depth in the z direction. (For interpretation of the references to color in this figure legend, the reader is referred to the Web version of this article.)

3.0:2.0, 1.0:1.0, and 1.0:4.0. Both the connected and unconnected percolated free volumes exist in the MPD/TMC ratio of 4.0:1.0, and the unconnected percolated free volume lies in the MPD/TMC ratio of 3.0:2.0, 1.0:1.0 and 1.0:4.0.

Supplementary video related to this article can be found at https://doi.org/10.1016/j.memsci.2022.120731

To further understand the role of connected or unconnected percolated free volume in water transport, we study the dynamic pore dimensions characterized by the accumulated free volume space. Fig. 9(b, d, f, h) show the accumulated percolated water-accessible volume space at z = 0L/4 Å, 1L/4 Å, 2L/4 Å, 3L/4 Å, and 4L/4 Å over 30 ns. The accumulated percolated free volume along z-direction has a notable difference for membranes with different MPD/TMC ratios at the same z-position. The membrane with an MPD/TMC ratio of 4.0:1.0 has the most accumulated free volume, followed by the ratio of 3.0:2.0, 1.0:1.0, and 1.0:4.0, which are directly related to water transport benefits. As illustrated in Fig. 9(a-h), it can find that PA membrane with the MPD/TMC ratio of 4.0:1.0 has both the continuum and non-continuum space, which indicate that water molecules pass through the membrane by continuum channels and the temporary on-and-off channels jumping from one cavity to another. However, membranes with MPD/TMC ratios of 3.0:2.0, 1.0:4.0, and 1.0:1.0 are more dependent on the temporary on-and-off channels jumping from one pore to another due to the dominated non-continuum space. These findings indicate that the water transport mechanism for PA membrane with different MPD/TMC ratios looks similar with some differences, which is also determined by the solution-diffusion model [95,96].

3.6. Effect of MPD/TMC ratio on pressure dependence of water desalination

Likewise, we first explore the pure water transport through the PA membranes with four MPD/TMC ratios at different pressure (from 30 to 150 MPa, Fig. S9(a-b)). Results show that the membrane with an MPD/TMC ratio of 4.0:1.0 has been destroyed at 120 and 150 MPa. Beyond that, both the permeated water molecules and water flux increase with the increasing pressure at the same MPD/TMC ratios, and gradually decrease as the MPD/TMC ratio changes from 1.0:4.0 to 1.0:1.0 to 3.0:2.0 to 4.0:1.0 at the same pressure. Water flux is also in accordance with the ideal pure water flux-pressure curve.

To further explore the effect of MPD/TMC ratio on pressure-driven water transport and salt rejection, we monitor the number of the permeated water molecules and rejected salt ions, water flux, rejection ratio and density profile of salt ions, and dynamic behavior of salt ions for membranes with four MPD/TMC ratio at different pressures. Fig. 10 (a) shows the number of water molecules passing through the membrane as a function of time for PA membranes with four MPD/TMC ratios at different pressures from 30 to 150 MPa, and the corresponding water flux per unit area per unit time as a function of pressure, are shown in Fig. 10(b). The number of the penetrated water molecules is almost linear with time after 5 ns. Membrane with the MPD/TMC ratio of 4.0:1.0 has been destroyed over 20 ns at both 120 and 150 MPa. Both the permeated water molecules and water flux increase with the increasing pressure for the membrane with the same MPD/TMC ratio. Under the same pressure, the membrane with an MPD/TMC ratio of 4.0:1.0 can permeate more water molecules and has an enormous water flux, followed by the ratio of 3.0:2.0, 1.0:1.0, and 1.0:4.0, which agrees well with their water-accessible space shown in Fig. 9(a-h). Comparing Fig. S9(a-b) with Fig. 10(a-b), after the introduction of salt ions, both the permeated water molecules and water flux are relatively smaller under the same MPD/TMC ratio and pressure, which suggest that salt ions can reduce the efficiency of water transport.

Returning to the salt ions transport, we first calculate the rejection ratio as shown in Fig. 10(c) using the rejected salt ions numbers (Fig. S10) over 30 ns for membranes with four MPD/TMC ratios at different pressures from 30 to 150 MPa. Membranes with an MPD/TMC ratio of 1.0:1.0, 1.0:4.0, and 3.0:2.0 can fully reject all salt ions within our simulation timescale. However, some salt ions can pass through the

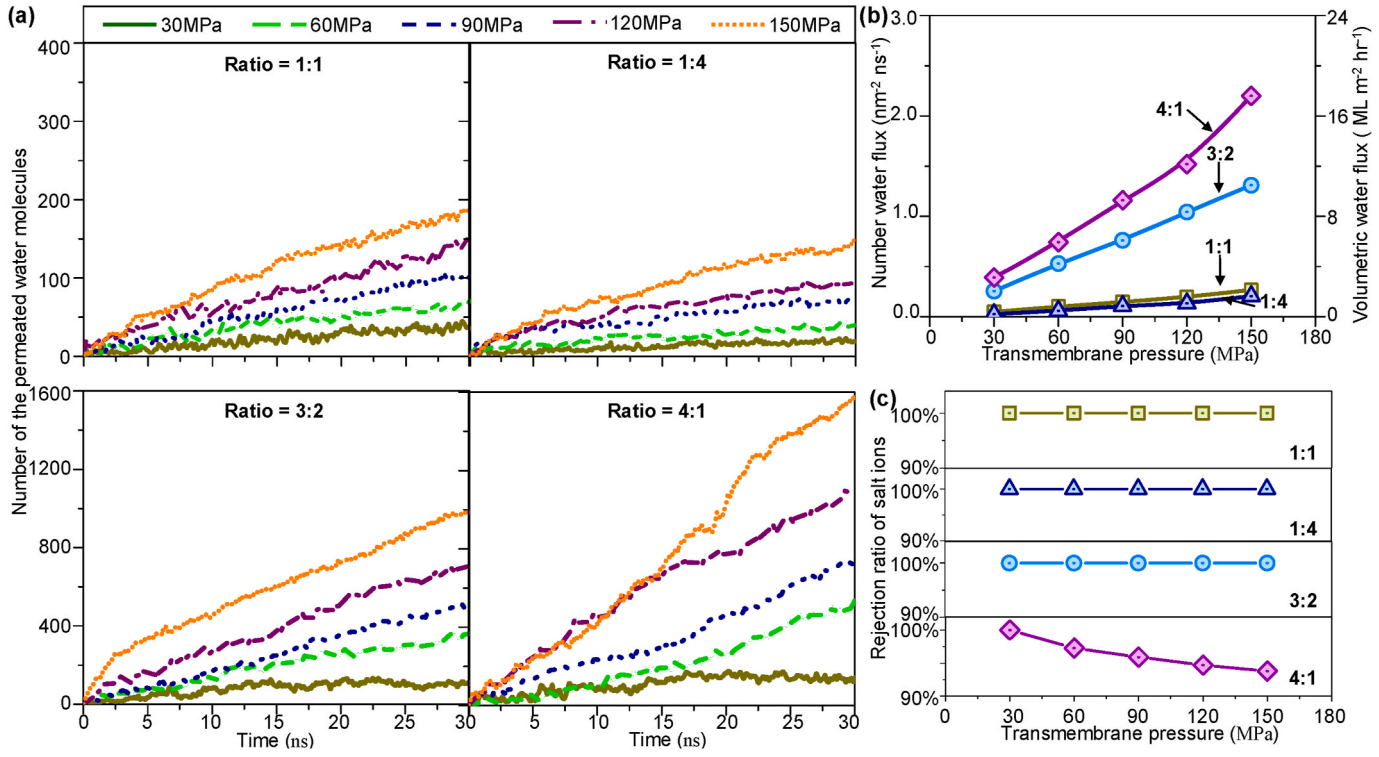

Fig. 10. Water transport through PA RO membranes with four MPD/TMC ratios, 1.0:1.0, 1.0:4.0, 3.0:2.0, and 4.0:1.0, under high saline conditions and high pressures (from 30 to 150 MPa). (a) Number of water molecules transported through the membrane as a function of simulation time at different pressures. (b) Water flux and (c) rejection of salt ions as a function of pressure for PA RO membranes with four MPD/TMC ratios.

membrane with an MPD/TMC ratio of 4.0:1.0, and both the rejected numbers of salt ions and rejection rate decrease with the increasing pressure, which can also be identified through the density profiles of salt ions (Na^+ and Cl^-, Fig. S11(a-b)) along *z*-direction before the pressure is applied (0 ns), and 30 ns after a 150 MPa pressure is imposed to the left graphene piston. These discoveries indicate that membranes with the MPD/TMC ratios of 1.0:1.0, 1.0:4.0, and 3.0:2.0 have a better performance than 4.0:1.0 for desalination. Next, we monitor the dynamics of the key salt ions (Fig. S12(a-l)) for membranes with different MPD/TMC ratios at 150 MPa. Results show that salt ions cost much time to move back and forth within the bulk water layer, and some salt ions can transport through the membrane along a gradient path for an MPD/TMC ratio of 4.0:1.0.

In addition, we analyze the microstructure of PA membranes with different MPD/TMC ratios at high pressure. Fig. 11 shows the PSD curves relating to the pore diameter for membranes with four MPD/TMC ratios at different pressures from 30 to 150 MPa. Obviously, as pressure increases, the pore space shows a considerable reduction at high pressure for membranes with MPD/TMC ratios of 1.0:1.0, 1.0:4.0, and 3.0:2.0, representing a compaction of the free volume and membrane thickness. Meanwhile, observing density profiles of the membranes with the four MPD/TMC ratios at different pressures (from 30 to 150 MPa, Fig. S13), it can find that more unreacted monomers are flushed out of the membrane surface and get into the bulk water for membrane with MPD/TMC ratio of 4.0:1.0. Membranes with MPD/TMC ratios of 1.0:1.0, 1.0:4.0, and 3.0:2.0 present more compact and uniform microstructural features than that of 4.0:1.0.

3.7. Pressure–dependent failure mechanism of PA membranes

As aforementioned, we find that PA membrane has been destroyed in the following circumstances: 40% DC at both 120 and 150 MPa, and 50% DC at 150 MPa, MPD/TMC ratio of 4.0:1.0 at both 120 and 150 MPa. To investigate the failure mechanism of PA membranes, we further analyze their stress-strain relationships. The initial model systems (obtained from 2.1) are first equilibrated through a 21-step MD equilibration protocol [97]. Based on the final equilibrium configuration, a simulation time of 2 ns is again carried out at 300 K and 0 MPa under the NPT ensemble. After equilibration, compressive deformation was implemented using the NEMD simulation. The z-dimension of the simulation box was reduced at each simulation step to develop constant strain rate deformation in a $N\sigma_{ij}\varepsilon_{ij}T$ ensemble, up to a maximum engineering compressive strain of 30%. The simulation system maintains zero pressure (0 MPa) along the x- and y-directions. Thus, the dimensions normal to the loading direction were free to change in response to Poisson's effect. The temperature was maintained at 300 K. The time step was 1.0 fs, and the engineering strain rate was $10^8\ s^{-1}$. The stress and strain are recorded at each step. As shown in Fig. 12(a, c), we plot the stress-strain relationships for PA membranes with different DCs and MPD/TMC ratios and then extract their corresponding yield strengths, as shown in Fig. 12(b, d). Fig. 12(b) shows the compressive yield strength as a function of different DCs. When the DC increases from 40% to 96%, the compressive yield strength increases from 100 to 430 MPa, an increase of 330%. We find that the yield strengths are about 100 and 135 MPa for PA membranes having the DC of 40% and 50%, respectively, which are below the corresponding applied pressure of 120 and 150 MPa. Fig. 12(d) shows the relationship between compressive yield strength of PA membrane and MPD/TMC ratios. Clearly, compressive yield strengths are 280 MPa, 160 MPa, 360 MPa and 95 MPa for PA membranes with MPD/TMC ratios of 1.0:1.0, 1.0:4.0, 3.2:2.0 and 4.0:1.0, respectively. Thus, the PA membrane with an MPD/TMC ratio of 4.0:1.0 is easily destroyed, when the external pressure exceeds 95 MPa.

4. Conclusion

In this study, using MD simulations, we systematically investigate the pressure–driven water, and salt transport through the 3D-printed PA RO membranes to explore the effects of DC and MPD/TMC ratio on their performance at the molecular level. We evaluate several performance metrics, including water flux, dynamic behaviors of water and salt ions, salt rejection, membrane density, microstructure, and local structural properties for seven DCs and four MPD/TMC ratios, and explain these findings using observations from both water molecules and salt ions transport dynamics and energetics.

At the microstructure level, different DCs and MPD/TMC ratios can dramatically affect the structural characteristics of PA membranes, including structural components, PSD, aromatic ring arrangement, and monomer spatial distribution, leading to the distinct pore space. Water flux is pressure-dependent, and the higher the external pressure, the faster water molecules permeate through the PA membrane. By optimizing pressure-dependent water flux, membrane structural features, and rejection, on one side, we find that PA membranes with an MPD/TMC ratio of 3.0:2.0 owns the best structural features as well as high water permeability and 100% salt rejection at high pressure within the simulation timescale. On the other side, 80%~90% is the optimal DC to maintain the excellent structural properties and keeps the total rejection for salt ions with the relatively large water permeability at high pressure.

In addition, no matter what DC or MPD/TMC ratio for 3D-printed PA RO membrane, water permeability is always associated with the percolated water-accessible free volume that provides a continuous path connecting the opposite membrane surfaces or the unconnected percolated free volume that allows water molecules to jump from one pore to another by the temporary on-and-off channels, or both the above two. However, salt ions also pass through the membrane via the continuous

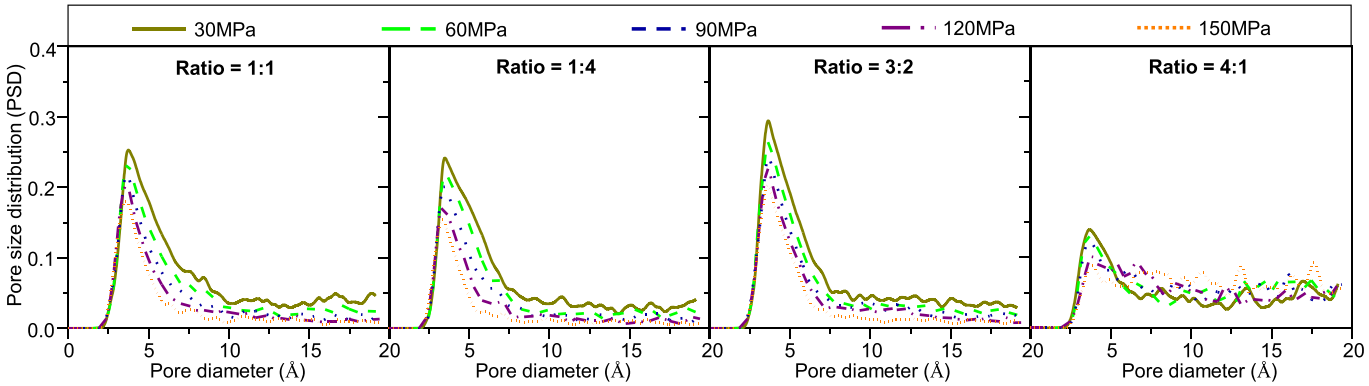

Fig. 11. Pore size distribution for PA RO membranes with four MPD/TMC ratios, 1.0:1.0, 1.0:4.0, 3.0:2.0, and 4.0:1.0, under different pressures from 30 to 150 MPa.

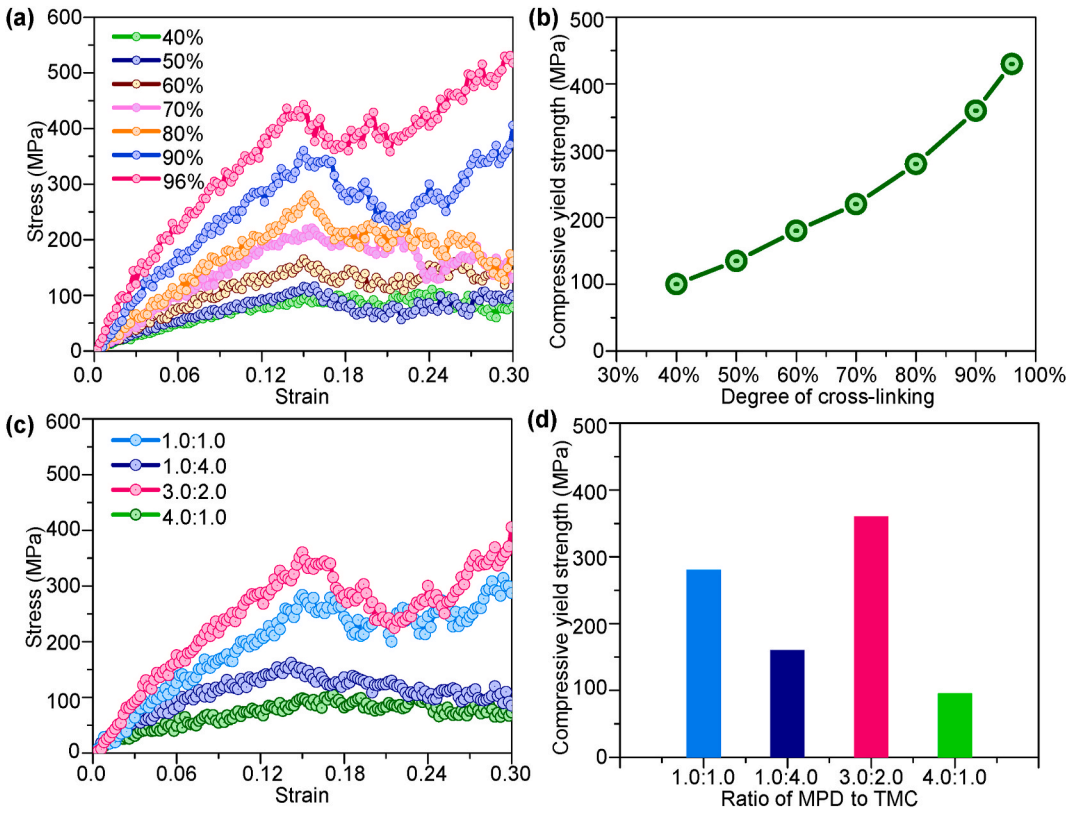

Fig. 12. (a) Stress-strain curves for uniaxial compressive loading of PA membranes with DC ranging from 40% to 96%, and (b) corresponding yield strengths as a function of DC. (c) Stress-strain curves of PA membranes with different MPD/TMC ratios under uniaxial compression loading, and (d) their corresponding yield strengths.

water channels. Importantly, we observe that the applied pressure, especially at high pressure, causes a rapid compaction of the free volume and membrane thickness for the highly crosslinked PA membrane. Moreover, we investigate that compressive yield strength for PA membranes increases with the increasing DC, while a 3:2 ratio of MPD/TMC maximized yield strength, which is an essential consideration for designing the high-pressure PA RO membranes.

These findings demonstrate how NEMD is a powerful method to deeply understand the influence of different synthesis conditions, such as DCs and MPD/TMC ratios, on pressure-driven water transport behaviors in 3D-printed PA RO membranes. Here, simulations are only limited to a membrane thickness of 50 Å, a timescale of tens of nanoseconds, and thousands of transported water molecules. The exploration of a wide range of membrane thickness with a larger simulation system over a longer timescale can clearly result in a better understanding for designing PA RO membranes at molecular level. Still, we expect that the molecular insights from this study will better guide the design and fabrication of precisely tuned 3D-printed PA RO membranes in water treatment and desalination.

Author statement

Jinlong He: Conceptualization, Methodology, Software, Validation, Formal analysis, Data curation, Writing – original draft, Visualization. Jason Yang: Conceptualization, Methodology, Software, Writing – review & editing. Jeffrey R McCutcheon: Conceptualization, Methodology, Supervision, Project administration, Funding acquisition. Ying Li: Conceptualization, Methodology, Software, Writing – review & editing, Supervision, Project administration, Funding acquisition.

Declaration of competing interest

The authors declare that they have no known competing financial interests or personal relationships that could have appeared to influence the work reported in this paper.

Acknowledgements

Y.L. and J.R.M would like to thank the support from the National Alliance for Water Innovation (NAWI), funded by the U.S. Department of Energy, Office of Energy Efficiency and Renewable Energy (EERE), Advanced Manufacturing Office, under Funding Opportunity Announcement Number DE-FOA-0001905. J.Y. would like to express thanks for the support by the U.S. National Science Foundation Graduate Research Fellowship Program under Grant No. 2021309491. Y.L. also gratefully acknowledges financial support from the U.S. National Science Foundation (CMMI-1762661, CMMI-1934829 and CAREER Award CMMI-2046751) and 3 M's Non-Tenured Faculty Award. Any opinion, findings, and conclusions or recommendations expressed in this material are those of the authors and do not necessarily reflect the views of the U. S. National Science Foundation and Department of Energy. This research also benefited in part from the computational resources and staff contributions provided by the Booth Engineering Center for Advanced Technology (BECAT) at the University of Connecticut. The authors also acknowledge the Texas Advanced Computing Center (TACC) at The University of Texas at Austin (Frontera project and National Science Foundation Award 1818253) and National Renewable Energy Laboratory (Eagle Computing System) for providing HPC resources that have contributed to the research results reported within this paper.

Appendix A. Supplementary data

Supplementary data to this article can be found online at https://doi.org/10.1016/j.memsci.2022.120731.

References

[1] M. Mekonnen Mesfin, Y. Hoekstra Arjen, Four billion people facing severe water scarcity, Sci. Adv., 2 e1500323.
[2] M.A. Shannon, P.W. Bohn, M. Elimelech, J.G. Georgiadis, B.J. Marinas, A. M. Mayes, Science and Technology for Water Purification in the Coming Decades, Nanoscience and Technology: a Collection of Reviews from Nature Journals, 2010, pp. 337–346.
[3] M. Elimelech, W.A. Phillip, The future of seawater desalination: energy, technology, and the environment, science 333 (2011) 712–717.
[4] M. Elimelech, A. Phillip William, The future of seawater desalination: energy, technology, and the environment, Science 333 (2011) 712–717.
[5] J.R. Werber, C.O. Osuji, M. Elimelech, Materials for next-generation desalination and water purification membranes, Nat. Rev. Mater. 1 (2016), 16018.
[6] K.P. Lee, T.C. Arnot, D. Mattia, A review of reverse osmosis membrane materials for desalination—development to date and future potential, J. Membr. Sci. 370 (2011) 1–22.
[7] J.E. Cadotte, R. Petersen, R. Larson, E. Erickson, A new thin-film composite seawater reverse osmosis membrane, Desalination 32 (1980) 25–31.
[8] J.E. Cadotte, R.J. Petersen, R.E. Larson, E.E. Erickson, A new thin-film composite seawater reverse osmosis membrane, Desalination 32 (1980) 25–31.
[9] B.-H. Jeong, E.M. Hoek, Y. Yan, A. Subramani, X. Huang, G. Hurwitz, A.K. Ghosh, A. Jawor, Interfacial polymerization of thin film nanocomposites: a new concept for reverse osmosis membranes, J. Membr. Sci. 294 (2007) 1–7.
[10] J.R. Werber, A. Deshmukh, M. Elimelech, The critical need for increased selectivity, not increased water permeability, for desalination membranes, Environ. Sci. Technol. Lett. 3 (2016) 112–120.
[11] B. Park Ho, J. Kamcev, M. Robeson Lloyd, M. Elimelech, D. Freeman Benny, Maximizing the right stuff: the trade-off between membrane permeability and selectivity, Science 356 (2017), eaab0530.
[12] H.B. Park, J. Kamcev, L.M. Robeson, M. Elimelech, B.D. Freeman, Maximizing the right stuff: the trade-off between membrane permeability and selectivity, Science 356 (2017), eaab0530.
[13] P.W. Morgan, S.L. Kwolek, Interfacial polycondensation. II. Fundamentals of polymer formation at liquid interfaces, J. Polym. Sci. 40 (1959) 299–327.
[14] T.E. Culp, B. Khara, K.P. Brickey, M. Geitner, T.J. Zimudzi, J.D. Wilbur, S.D. Jons, A. Roy, M. Paul, B. Ganapathysubramanian, Nanoscale control of internal inhomogeneity enhances water transport in desalination membranes, Science 371 (2021) 72–75.
[15] T.E. Culp, Y.-x. Shen, M. Geitner, M. Paul, A. Roy, M.J. Behr, S. Rosenberg, J. Gu, M. Kumar, E.D. Gomez, Electron tomography reveals details of the internal microstructure of desalination membranes, Proc. Natl. Acad. Sci. USA 115 (2018) 8694–8699.
[16] H. An, J.W. Smith, B. Ji, S. Cotty, S. Zhou, L. Yao, F.C. Kalutantirige, W. Chen, Z. Ou, X. Su, J. Feng, Q. Chen, Mechanism and performance relevance of nanomorphogenesis in polyamide films revealed by quantitative 3D imaging and machine learning, Sci. Adv. 8 (2022), eabk1888.
[17] A.K. Ghosh, E.M.V. Hoek, Impacts of support membrane structure and chemistry on polyamide–polysulfone interfacial composite membranes, J. Membr. Sci. 336 (2009) 140–148.
[18] V. Freger, Nanoscale heterogeneity of polyamide membranes formed by interfacial polymerization, Langmuir 19 (2003) 4791–4797.
[19] A.D. Khawaji, I.K. Kutubkhanah, J.-M. Wie, Advances in seawater desalination technologies, Desalination 221 (2008) 47–69.
[20] O. Coronell, B.J. Mariñas, D.G. Cahill, Depth heterogeneity of fully aromatic polyamide active layers in reverse osmosis and nanofiltration membranes, Environ. Sci. Technol. 45 (2011) 4513–4520.
[21] F. Pacheco, R. Sougrat, M. Reinhard, J.O. Leckie, I. Pinnau, 3D visualization of the internal nanostructure of polyamide thin films in RO membranes, J. Membr. Sci. 501 (2016) 33–44.
[22] E. Culp Tyler, B. Khara, P. Brickey Kaitlyn, M. Geitner, J. Zimudzi Tawanda, D. Wilbur Jeffrey, D. Jons Steven, A. Roy, M. Paul, B. Ganapathysubramanian, L. Zydney Andrew, M. Kumar, D. Gomez Enrique, Nanoscale control of internal inhomogeneity enhances water transport in desalination membranes, Science 371 (2021) 72–75.
[23] H. An, J.W. Smith, W. Chen, Z. Ou, Q. Chen, Charting the quantitative relationship between two-dimensional morphology parameters of polyamide membranes and synthesis conditions, Mol. Syst. Design Eng. 5 (2020) 102–109.
[24] X. Song, J.W. Smith, J. Kim, N.J. Zaluzec, W. Chen, H. An, J.M. Dennison, D. G. Cahill, M.A. Kulzick, Q. Chen, Unraveling the morphology–function relationships of polyamide membranes using quantitative electron tomography, ACS Appl. Mater. Interfaces 11 (2019) 8517–8526.
[25] J.-E. Gu, S. Lee, C.M. Stafford, J.S. Lee, W. Choi, B.-Y. Kim, K.-Y. Baek, E.P. Chan, J. Y. Chung, J. Bang, J.-H. Lee, Molecular layer-by-layer assembled thin-film composite membranes for water desalination, Adv. Mater. 25 (2013) 4778–4782.
[26] S. Karan, Z. Jiang, G. Livingston Andrew, Sub–10 nm polyamide nanofilms with ultrafast solvent transport for molecular separation, Science 348 (2015) 1347–1351.
[27] F. Perreault, M.E. Tousley, M. Elimelech, Thin-film composite polyamide membranes functionalized with biocidal graphene oxide nanosheets, Environ. Sci. Technol. Lett. 1 (2014) 71–76.
[28] R. Chowdhury Maqsud, J. Steffes, D. Huey Bryan, R. McCutcheon Jeffrey, 3D printed polyamide membranes for desalination, Science 361 (2018) 682–686.
[29] X. Qian, M. Ostwal, A. Asatekin, G.M. Geise, Z.P. Smith, W.A. Phillip, R.P. Lively, J. R. McCutcheon, A critical review and commentary on recent progress of additive manufacturing and its impact on membrane technology, J. Membr. Sci. (2021), 120041.
[30] X. Qian, M. Ostwal, A. Asatekin, G.M. Geise, Z.P. Smith, W.A. Phillip, R.P. Lively, J. R. McCutcheon, A critical review and commentary on recent progress of additive manufacturing and its impact on membrane technology, J. Membr. Sci. 645 (2022) 120041.
[31] S. Karan, Z. Jiang, A.G. Livingston, Sub–10 nm polyamide nanofilms with ultrafast solvent transport for molecular separation, Science 348 (2015) 1347–1351.
[32] Z. Jiang, S. Karan, A.G. Livingston, Water transport through ultrathin polyamide nanofilms used for reverse osmosis, Adv. Mater. 30 (2018), 1705973.
[33] V. Freger, G.Z. Ramon, Polyamide desalination membranes: formation, structure, and properties, Prog. Polym. Sci. 122 (2021), 101451.
[34] J. Muscatello, E. Müller, A. Mostofi, A. Sutton, Multiscale molecular simulations of the formation and structure of polyamide membranes created by interfacial polymerization, J. Membr. Sci. 527 (2017) 180–190.
[35] A.K. Ghosh, B.-H. Jeong, X. Huang, E.M. Hoek, Impacts of reaction and curing conditions on polyamide composite reverse osmosis membrane properties, J. Membr. Sci. 311 (2008) 34–45.
[36] R. Nadler, S. Srebnik, Molecular simulation of polyamide synthesis by interfacial polymerization, J. Membr. Sci. 315 (2008) 100–105.
[37] A.V. Berezkin, Y.V. Kudryavtsev, Effect of cross-linking on the structure and growth of polymer films prepared by interfacial polymerization, Langmuir 31 (2015) 12279–12290.
[38] A.F. Ismail, T. Matsuura, Progress in transport theory and characterization method of Reverse Osmosis (RO) membrane in past fifty years, Desalination 434 (2018) 2–11.
[39] H.F. Ridgway, J. Orbell, S. Gray, Molecular simulations of polyamide membrane materials used in desalination and water reuse applications: recent developments and future prospects, J. Membr. Sci. 524 (2017) 436–448.
[40] M. Ding, Molecular simulations of reverse osmosis membranes, Rennes 1 (2015).
[41] M. Ding, A. Szymczyk, A. Ghoufi, Hydration of a polyamide reverse-osmosis membrane, J. Membr. Sci. 501 (2016) 248–253.
[42] V. Kolev, V. Freger, Molecular dynamics investigation of ion sorption and permeation in desalination membranes, J. Phys. Chem. B 119 (2015) 14168–14179.
[43] V. Kolev, V. Freger, Hydration, porosity and water dynamics in the polyamide layer of reverse osmosis membranes: a molecular dynamics study, Polymer 55 (2014) 1420–1426.
[44] M. Shen, S. Keten, R.M. Lueptow, Dynamics of water and solute transport in polymeric reverse osmosis membranes via molecular dynamics simulations, J. Membr. Sci. 506 (2016) 95–108.
[45] H. Zhang, M.S. Wu, K. Zhou, A.W.-K. Law, Molecular insights into the composition–structure–property relationships of polyamide thin films for reverse osmosis desalination, Environ. Sci. Technol. 53 (2019) 6374–6382.
[46] D.M. Davenport, A. Deshmukh, J.R. Werber, M. Elimelech, High-pressure reverse osmosis for energy-efficient hypersaline brine desalination: current status, design considerations, and research needs, Environ. Sci. Technol. Lett. 5 (2018) 467–475.
[47] D.M. Davenport, C.L. Ritt, R. Verbeke, M. Dickmann, W. Egger, I.F. Vankelecom, M. Elimelech, Thin film composite membrane compaction in high-pressure reverse osmosis, J. Membr. Sci. 610 (2020), 118268.
[48] D.M. Davenport, L. Wang, E. Shalusky, M. Elimelech, Design principles and challenges of bench-scale high-pressure reverse osmosis up to 150 bar, Desalination 517 (2021), 115237.
[49] S. Huang, J. Mansouri, P. Le-Clech, G. Leslie, C.Y. Tang, A.G. Fane, A comprehensive review of electrospray technique for membrane development: current status, challenges, and opportunities, J. Membr. Sci. (2022), 120248.
[50] W. Humphrey, A. Dalke, K. Schulten, VMD: visual molecular dynamics, J. Mol. Graph. 14 (1996) 33–38.
[51] E.L. Wittbecker, P.W. Morgan, Interfacial polycondensation. I, J. Polym. Sci. 40 (1959) 289–297.
[52] C. Jang, T.W. Sirk, J.W. Andzelm, C.F. Abrams, Comparison of crosslinking algorithms in molecular dynamics simulation of thermosetting polymers, Macromol. Theory Simul. 24 (2015) 260–270.
[53] S. Qiu, L. Wu, L. Zhang, H. Chen, C. Gao, Preparation of reverse osmosis composite membrane with high flux by interfacial polymerization of MPD and TMC, J. Appl. Polym. Sci. 112 (2009) 2066–2072.
[54] L.J. Abbott, K.E. Hart, C.M. Colina, Polymatic: a generalized simulated polymerization algorithm for amorphous polymers, Theor. Chem. Acc. 132 (2013) 1–19.
[55] M. Shen, S. Keten, R. Lueptow, Dynamics of water and solute transport in polymeric reverse osmosis membranes via molecular dynamics simulations, J. Membr. Sci. 506 (2016).
[56] M. Ding, A. Szymczyk, F. Goujon, A. Soldera, A. Ghoufi, Structure and dynamics of water confined in a polyamide reverse-osmosis membrane: a molecular-simulation study, J. Membr. Sci. 458 (2014) 236–244.
[57] M. Kotelyanskii, N. Wagner, M. Paulaitis, Molecular dynamics simulation study of the mechanisms of water diffusion in a hydrated, amorphous polyamide, Comput. Theor. Polym. Sci. 9 (1999) 301–306.

[58] E. Jones, M. Qadir, M.T. van Vliet, V. Smakhtin, S.-m. Kang, The state of desalination and brine production: a global outlook, Sci. Total Environ. 657 (2019) 1343–1356.
[59] E. Harder, D.E. Walters, Y.D. Bodnar, R.S. Faibish, B. Roux, Molecular dynamics study of a polymeric reverse osmosis membrane, J. Phys. Chem. B 113 (2009) 10177–10182.
[60] J. Yang, Z. Shen, J. He, Y. Li, Efficient separation of small organic contaminants in water using functionalized nanoporous graphene membranes: insights from molecular dynamics simulations, J. Membr. Sci. 630 (2021), 119331.
[61] M. Ding, A. Szymczyk, A. Ghoufi, On the structure and rejection of ions by a polyamide membrane in pressure-driven molecular dynamics simulations, Desalination 368 (2015) 76–80.
[62] W. Gao, F. She, J. Zhang, L.F. Dumée, L. He, P.D. Hodgson, L. Kong, Understanding water and ion transport behaviour and permeability through poly(amide) thin film composite membrane, J. Membr. Sci. 487 (2015) 32–39.
[63] M.J. Kotelyanskii, N.J. Wagner, M.E. Paulaitis, Molecular dynamics simulation study of the mechanisms of water diffusion in a hydrated, amorphous polyamide, Comput. Theor. Polym. Sci. 9 (1999) 301–306.
[64] H. Sun, S.J. Mumby, J.R. Maple, A.T. Hagler, An ab initio CFF93 all-atom force field for polycarbonates, J. Am. Chem. Soc. 116 (1994) 2978–2987.
[65] H. Sun, Ab initio calculations and force field development for computer simulation of polysilanes, Macromolecules 28 (1995) 701–712.
[66] H. Heinz, T.-J. Lin, R. Kishore Mishra, F.S. Emami, Thermodynamically consistent force fields for the assembly of inorganic, organic, and biological nanostructures: the INTERFACE force field, Langmuir 29 (2013) 1754–1765.
[67] H. Sun, COMPASS: an ab initio force-field optimized for condensed-phase applications overview with details on alkane and benzene compounds, J. Phys. Chem. B 102 (1998) 7338–7364.
[68] S. Plimpton, Fast Parallel algorithms for short-range molecular dynamics, J. Comput. Phys. 117 (1995) 1–19.
[69] S. Liu, S. Ganti-Agrawal, S. Keten, R.M. Lueptow, Molecular insights into charged nanofiltration membranes: structure, water transport, and water diffusion, J. Membr. Sci. 644 (2022) 120057.
[70] R. Vickers, T.M. Weigand, C.T. Miller, O. Coronell, Molecular methods for assessing the morphology, topology, and performance of polyamide membranes, J. Membr. Sci. 644 (2022), 120110.
[71] W. Zhang, R. Chu, W. Shi, Y. Hu, Quantitively unveiling the activity-structure relationship of polyamide membrane: a molecular dynamics simulation study, Desalination 528 (2022), 115640.
[72] S. Nosé, A unified formulation of the constant temperature molecular dynamics methods, J. Chem. Phys. 81 (1984) 511–519.
[73] W.G. Hoover, Canonical dynamics: equilibrium phase-space distributions, Phys. Rev. 31 (1985) 1695–1697.
[74] J. Muscatello, E.A. Müller, A.A. Mostofi, A.P. Sutton, Multiscale molecular simulations of the formation and structure of polyamide membranes created by interfacial polymerization, J. Membr. Sci. 527 (2017) 180–190.
[75] W. Wei, J. Liu, J. Jiang, Atomistic simulation study of polyarylate/zeolitic-imidazolate framework mixed-matrix membranes for water desalination, ACS Appl. Nano Mater. 3 (2020) 10022–10031.
[76] H. Chan, M.J. Cherukara, B. Narayanan, T.D. Loeffler, C. Benmore, S.K. Gray, S. K. Sankaranarayanan, Machine learning coarse grained models for water, Nat. Commun. 10 (2019) 1–14.
[77] B. Mi, O. Coronell, B.J. Mariñas, F. Watanabe, D.G. Cahill, I. Petrov, Physico-chemical characterization of NF/RO membrane active layers by Rutherford backscattering spectrometry, J. Membr. Sci. 282 (2006) 71–81.
[78] M.J. Kotelyanskii, N.J. Wagner, M.E. Paulaitis, Atomistic simulation of water and salt transport in the reverse osmosis membrane FT-30, J. Membr. Sci. 139 (1998) 1–16.
[79] J. Lee, C.M. Doherty, A.J. Hill, S.E. Kentish, Water vapor sorption and free volume in the aromatic polyamide layer of reverse osmosis membranes, J. Membr. Sci. 425–426 (2013) 217–226.
[80] T. Huang, B.A. Moosa, P. Hoang, J. Liu, S. Chisca, G. Zhang, M. AlYami, N. M. Khashab, S.P. Nunes, Molecularly-porous ultrathin membranes for highly selective organic solvent nanofiltration, Nat. Commun. 11 (2020) 1–10.
[81] Q. Fu, N. Verma, H. Ma, F.J. Medellin-Rodriguez, R. Li, M. Fukuto, C.M. Stafford, B. S. Hsiao, B.M. Ocko, Molecular structure of aromatic reverse osmosis polyamide barrier layers, ACS Macro Lett. 8 (2019) 352–356.
[82] H. Peng, W.H. Zhang, W.S. Hung, N. Wang, J. Sun, K.R. Lee, Q.F. An, C.M. Liu, Q. Zhao, Phosphonium modification leads to ultrapermeable antibacterial polyamide composite membranes with unreduced thickness, Adv. Mater. 32 (2020), 2001383.
[83] L. Sarkisov, R. Bueno-Perez, M. Sutharson, D. Fairen-Jimenez, Materials informatics with PoreBlazer v4.0 and the CSD MOF database, Chem. Mater. 32 (2020) 9849–9867.
[84] D. Xu, Y. Zhang, Generating triangulated macromolecular surfaces by Euclidean distance transform, PLoS One 4 (2009), e8140.
[85] M. Gerstein, C. Chothia, Packing at the protein-water interface, Proc. Natl. Acad. Sci. USA 93 (1996) 10167–10172.
[86] S.H. Kim, S.-Y. Kwak, T. Suzuki, Positron annihilation spectroscopic evidence to demonstrate the flux-enhancement mechanism in morphology-controlled thin-film-composite (TFC) membrane, Environ. Sci. Technol. 39 (2005) 1764–1770.
[87] T.Z. Hong, L. You, M. Dahanayaka, A.W. Law, K. Zhou, Influence of substitutional defects in ZIF-8 membranes on reverse osmosis desalination: a molecular dynamics study, Molecules (2021) 26.
[88] Y. Yoon, R.M. Lueptow, Removal of organic contaminants by RO and NF membranes, J. Membr. Sci. 261 (2005) 76–86.
[89] R.I. Urama, B.J. Mariñas, Mechanistic interpretation of solute permeation through a fully aromatic polyamide reverse osmosis membrane, J. Membr. Sci. 123 (1997) 267–280.
[90] K.H. Chu, J.S. Mang, J. Lim, S. Hong, M.-H. Hwang, Variation of free volume and thickness by high pressure applied on thin film composite reverse osmosis membrane, Desalination 520 (2021), 115365.
[91] S. Karan, Z. Jiang, A. Livingston, MEMBRANE FILTRATION. Sub-10 nm polyamide nanofilms with ultrafast solvent transport for molecular separation, Science 348 (2015) 1347–1351.
[92] C.R. Martinez, B.L. Iverson, Rethinking the term “pi-stacking”, Chem. Sci. 3 (2012) 2191–2201.
[93] T. Wei, M.S.J. Sajib, M. Samieegohar, H. Ma, K. Shing, Self-assembled monolayers of an azobenzene derivative on silica and their interactions with lysozyme, Langmuir 31 (2015) 13543–13552.
[94] T. Wei, L. Zhang, H. Zhao, H. Ma, M.S.J. Sajib, H. Jiang, S. Murad, Aromatic polyamide reverse-osmosis membrane: an atomistic molecular dynamics simulation, J. Phys. Chem. B 120 (2016) 10311–10318.
[95] C. Hannesschlaeger, A. Horner, P. Pohl, Intrinsic membrane permeability to small molecules, Chem. Rev. 119 (2019) 5922–5953.
[96] J.G. Wijmans, R.W. Baker, The solution-diffusion model: a review, J. Membr. Sci. 107 (1995) 1–21.
[97] L.J. Abbott, K.E. Hart, C.M. Colina, Polymatic: a generalized simulated polymerization algorithm for amorphous polymers, Theor. Chem. Acc. 132 (2013) 1334.